NON-LINEAR OPTICAL METHODS TO UNDERSTAND PATHOPHYSIOLOGY OF SMALL BLEEDS

A Dissertation

Presented to the Faculty of the Graduate School

of Cornell University

In Partial Fulfillment of the Requirements for the Degree of

Doctor of Philosophy

by

Sung Ji Ahn

December 2017

NON-LINEAR OPTICAL METHODS TO UNDERSTAND PATHOPHYSIOLOGY OF SMALL BRAIN BLEEDS

Sung Ji Ahn, Ph. D.

Cornell University 2017

Cerebral microhemorrhages (CMBs) are small hemorrhagic strokes found in the brain, also known as silent stroke since they do not illicit noticeable symptoms. Recently, due to the development of various imaging modalities and aging population in the western world, increasing number of CMBs are detected. Clinical studies have shown that aging and hypertension significantly increases the chance of such bleeds and the National Institute of Health recognizes CMBs as a major factor in Alzheimer disease pathology. Independent events of CMBs are also a risk factor for subsequent larger intracerebral hemorrhages, ischemic stroke, Binswager's disease and Alzheimer's disease. However, studies in cellular level are lacking, partially due to inadequate animal model that allow both detection and follow up analysis of such small bleeds. We used tightly focused femtosecond laser pulses to injure single penetrating arterioles in the cortex of live anesthetized rodents and used multi-photon excited fluorescence imaging to quantify inflammatory responses over long periods of time. The work presented in this dissertation provides comprehensive spatial and temporal pathological consequences after micro scale hemorrhagic injury to a single blood vessel in the brain.

BIOGRAPHICAL SKETCH

Sung Ji Ahn was born in Busan, South Korea in 1987. She spent her childhood in Daeduk Research Complex, also known as Korea's Silicon Valley. Surrounded with people chasing scholastic and intellectual value, she grew up with the ambition to pursue a scientific career as a biological scientist. In 2006, she attended Hanyang University in Seoul, South Korea majoring in Biomedical Engineering. During her junior year in college, she spent one year studying abroad in University of Texas at Austin. She conducted research in designing neural grafts that use an electrical cue to aid regeneration of peripheral nervous tissue under the guidance of Dr. Christine E Schmidt. Fascinated by how neurons wire up with precision and change their connection for a purpose, her second research position was at The University of Texas Medical School in Houston under the guidance of Dr. John H. Byrne where she observed that repeated axonal conduction could change the strength of synaptic connection via protein synthesis. In February of 2010, she graduated from Hanyang University with Summa Cum Laude. She then extended her study in neuroscience at the Neurophysiology lab in Seoul National University (SNU). Under the guidance of Dr. Sang Jeong Kim, she studied molecular mechanism on cerebellar long-term depression (LTD), which underlies motor coordination and associative learning. In August of 2012, Sung Ji attended Cornell University as a Ph.D. candidate in the field of Biomedical Engineering with the hope of explaining inflammatory responses in brain that hinders with neural engineering approaches (i.e. chip implantation, electrophysiological recordings) and underlies various neurodegenerative diseases. She joined Dr. Chris Schaffer's laboratory where she spent the past five and half years studying the inflammatory responses due to microbleeds and identify the role of microglia, the first and main form of active immune defense in brain.

To my family and friends

ACKNOWLEDGMENTS

This dissertation was made possible by everyone I met here at Ithaca and back at home in Korea, whom directly or indirectly influenced me throughout the whole fulfilling graduate experience.

I would like to express my sincere, utmost gratitude to individuals who had the deepest impact on me. First, to my advisor Dr. Chris Schaffer, I greatly appreciate his endless patience, comprehensive supervision and shaping a well-rounded PhD experience for me. Chris has always encouraged and supported me to pursue and follow my widespread scientific curiosity by giving a room to explore within a comfort zone. Each of those trial-and-errors was priceless with great learning values in the end. I still have so much to learn from him in both technical and communication skills, which will be continued throughout the rest of my scientific career. I also want to thank Dr. Nozomi Nishimura for always listening, offering support and guidance over the years and teaching me critical skillsets such as craniotomy, inducing clots and hemorrhages with femtosecond laser that I am very grateful of. I would like to thank Dr. Avery August and Dr. Alyosha Molnar for their warmhearted supports and advises as the member of my thesis committee. They helped me to coincide my education to my research goal, where I familiarized myself with immunology and optics, which helped me greatly throughout my degree. I also want to thank my collaborator Dr. Josef Anrather down at Weill Cornell medical school for his collaboration and advice over the years.

I would like to thank all members of the Schaffer-Nishimura lab. Starting from Jiahn, for all those time together with support, encouragement and endless night of spirits

and laughter. Amanda and JC both of whom I had immense scientific and non-scientific conversations with, which made my time in the lab enjoyable in so much different ways. Amanda taught me proper English and influenced me to adhere to rules and norms. JC influenced me to live a healthy life with regular workouts. I especially enjoyed JC's humor and sociability. Liz and Poornima greatly influenced me during my early years of PhD. Liz was confident strong figure whom always heartily listened whenever I was frustrated and helped me restore my confidence. I enjoyed working with Poornima in the laser room and watching Indian movies late at night in the office. She would always align ablation laser so perfectly, so that I didn't even need to worry at all. Jason heartily cared any issues I encountered and critically helped me through machining ear bars and fixing microscope. Dr. Oliver Bracko and Dr. David Small for being scientific mentor and putting up with my endless questions. You guys always rescued me when I was struggling with scientific adversities by directing and teaching me new techniques with genuine encouragements. My last part of PhD was so productive and efficient, thanks to both of you. Yuting for the fun times that made my time in lab so entertaining, although you didn't intend to. Mohammad, Sally, Yiming, Mitch, Menansili, Silvia, Daniel, Nancy, John and many other undergraduate students, thank you for putting up with me when I was frustrated and cheering with me when things worked. Together with Chris, Nozomi and dynamic, energetic and entertaining lab members, I experienced endless adventures in the mountains and the sea, in which I would have not attempted.

I have been fortunate enough to work with inspiring collaborators that have also made my time at Cornell gratifying and rewarding. Special thanks to Dr. Xiaolai Zhou and

Dr. Fenghua Hu for scientific discussion and months of collaboration on revealing microglia physiology in Alzheimer's disease. Collaboration with Xu lab - Tianyu, Chunyan and Dr. Dimitre Ouzounov. Together we imaged deep in the brain!!

I would also like to acknowledge people I met outside the lab. Special thanks to Bo Ri, Younghye, Soojin, Suwon, Junghun and Minji for their support and love, the valuable board members of Korean Graduate Association at Cornell 13-14, and members of Cornell Korean Tennis Club.

Last but not least, I would also like to thank my loving parents and brother Woojin for always supporting my decisions and embracing my accomplishments. Seunghwan, thank you for being part of this journey.

TABLE OF CONTENTS

LIST OF FIGURES

LIST OF ABBREVIATIONS

THG	third harmonic generation
ApoE	apolipoprotein
2PEF	two-photon excitation fluorescence
3PEF	three-photon excitation fluorescence
MPEF	multi-photon excitation fluorescence
NA	numerical aperture
HG	harmonic generation
SHG	second harmonic generation
THG	third harmonic generation
PMT	photomultiplier tube
CMBs	cerebral microbleeds
CT	computed tomography
MRI	magnetic resonance imaging
GRE	gradient recalled echo
SWI	susceptibility-weighted imaging
CADASIL	cerebral autosomal-dominant arteriopathy
CAA	cerebral amyloid angiopathy
ICH	intracerebral hemorrhage
MARS	microbleed anatomical rating scale
BMT	bone marrow transplant
GFP	green fluorescent protein

RFP	red fluorescent protein
EdU	5-ethynyl-2’-deoxyuridine
BBB	brain blood barrier
GFAP	glial fibrillary acidic protein
IL-1β	interleukin-1beta
LTP	long term potentiation
TNFα	tumor necrosis factor-α
AMPA	α-amino-3-hydroxy-5-methyl-4-isoxazolepropionic acid
IL-1α	interleukin 1 alpha
C1q	complement component subunit 1q
RBCs	red blood cells
FITC	fluorescein isothiocyanate
OPA	optical parametric amplifier
WM	white matter
VCID	vascular cognitive impairment and dementia
CBF	cerebral blood flow
CC	corpus callosum
BCAS	bilateral common carotid artery stenosis
ASL	arterial spin labeled
ATP	adenosine triphosphate

CHAPTER ONE

INTRODUCTION AND ORGANIZATION OF DISSERTATION

1.1 Introduction

The work described in this dissertation involves the study of neuropathology using various optical methods to modulate and/or observe various structures in the brain. Each chapter can be read independently.

Chapter 2

This chapter provides an introduction on nonlinear imaging, specifically multi-photon excited fluorescence used for *in vivo* imaging in this dissertation. The chapter describes the physics behind multi-photon excited fluorescence, its advantage over single photon excited fluorescence imaging, implications in biological research and its applications. This chapter also introduces higher harmonic generations and femtosecond laser induced ionization techniques to rupture a blood vessel or selectively ablate targeted cell types in the brain.

Chapter 3

This chapter introduces cerebral microbleeds by compiling recent literature. Topics range from the definition of cortical microbleeds, how they are detected, clinical implications, and the underlying pathophysiology at the cellular and systemic level.

Chapter 4

This chapter provides a comprehensive picture of the inflammatory response following microhemorrhage. This chapter primarily focuses on the identification of major inflammatory cell types and their spatiotemporal dynamics following lesions. To

understand the mechanisms leading to increased inflammatory cell density near the lesion, a computational simulation is presented to further understand the coordinated pattern of cell migration and proliferation due to microhemorrhage.

Chapter 5

This chapter introduces label free measurement of cortical blood cell speed using third harmonic generation (THG) microscopy. A comparison of blood cell speed with and without a vascular fluorescent dye measured by line scan technique is presented.

Chapter 6

This chapter explores the influence of the apolipoprotein E4 (ApoE4) on blood flow within the corpus callosum white matter. Using three-photon fluorescence microscopy with third harmonic generation, we measure blood cell speed in the capillaries located in the white matter. We demonstrate that the expression of ApoE4 decreases blood flow in the white matter that is exacerbated with a model of diffuse white matter injury.

Chapter 7

This chapter provides a summary of important findings presented by this thesis. Possible future directions to further define the influence of blood flow alterations to the pathophysiology of the brain, are also discussed.

CHAPTER TWO

NONLINEAR OPTICAL METHODS TO IMAGE AND MANIPULATE BIOLOGICAL SYSTEMS

2.1 Multiphoton Microscopy for Biological Studies

Over the past decades, along with the advances in the molecular biology, genomics and proteomics revolutions, optical microscopy has become one of the most important research tool used in biomedical research [1]. For example, genetic targeting strategies can express structural and functional fluorescent proteins with cellular specificity in a living animal. These proteins can yield highly-quantitative data which indirectly probe molecular kinetics, pH, and calcium transients to using the emitted fluorescent signal. Therefore, the multiphoton microscope has become the go to tool to answer quantitative biological questions. Nonlinear microscopy gains multiple advantages over linear confocal microscopy through restricting the fluorescence excitation volume, rather than restricting the fluorescence collection to localize the fluorescent signal in space, allowing for optical sectioning. This efficiency allowed deep imaging through scattering tissue with high resolution and contrast and lowers the chance of photo bleaching and secondary laser induced damage. Therefore, the advent of nonlinear microscopy opened an era of imaging living animals in a minimally invasive way to study the cellular structures and processes, allowing study of their response to systematic manipulations in their natural environment.

2.1.1 Multiphoton Excitation Fluorescence

Fluorescence occurs when a fluorophore absorbs a photon, raising an electron to an excited energy state, from which it relaxes back to the electronic ground state and emits a lower energy photon. The absorption occurs when the energy of a laser photon is equal to or greater than the energy difference between the two states. The minimum

energy that can transit a fluorophore from ground state to higher excited state depends on the nature of fluorophore, and this energy can be given by a single or by multiple photons. The energy of a photon is inversely proportional to its wavelength ($E = \frac{hc}{\lambda}$, where h is Planck's constant, c is speed of light, and λ is wavelength). Thus,, multiple photons of longer wavelengths can generate the same amount of energy as a single photon of shorter wavelength.

Two-photon excitation fluorescence (2PEF) refers to the excitation of a fluorophore when two photons arrive within a time window of an attosecond (10^{-18} s) and excite a fluorescent molecule [2]. Any combination of photons of with the net sum can work, but for practical reasons, two photons of same energy are typically used. The same principle applies to three-photon excitation fluorescence (3PEF), by simultaneously using three photons to team up to excite one molecule. Multi-photon excitation fluorescence (MEF) requires extremely high photon flux for simultaneous absorption of multiple photons to achieve fluorescence. To achieve sufficient MEF while preserving the integrity of biological tissue, pulsed light is used. A mode locked laser can emits intermittently in high intensity bursts rather than in a continuous beam. Generally, picosecond to femtosecond duration pulses with low repetition rate (<100 MHz) is used for excitation source. Furthermore, the 3PEF excitation volume is more tightly focused than 2PEF as 3PEF falls off from the focal plane as ~ $1/z^4$ (z is the distance), while 2PEF falls off as ~ $1/z^2$ [3]. The pulsed laser beam is spatially constrained to a diffraction-limited volume by using a high-numerical aperture (NA) microscope objective. When a laser beam is tightly focused inside a fluorescent sample, the peak intensity will be at the

focus and thus the resulting image will have less out-of-focus background in regions far away from the focal plane.

2.1.2 Harmonic Generation

Harmonic generation is a coherent (phase-preserving) process that requires no actual absorption but generates output signal near a resonant material. Optical harmonic generation uses two or three photons simultaneously to create a single photon of exactly twice (or triple, based on the order of the harmonic) the incoming energy from the excitation photon. Therefore, the laser-induced harmonic generation (HG) deposits no energy in the material. It can provide noninvasive optical imaging ideal for some clinical uses [4]. HG utilizes endogenous structure in a biological sample (label-free imaging) and doesn't require a fluorophore to generate a signal; it can avoid common issues of fluorescence excitation, such as photodamage, phototoxicity, photobleaching, and dye toxicity. HG in biological imaging includes second harmonic generation (SHG), and third harmonic generation (THG) based on the material properties, both can be generated with a sufficiently compressed laser pulse.

The following second order equation can describe SHG, where $\chi^{(2)}(2\omega{:}\,\omega,\omega)$ is the susceptibility tensor that converts two photons of incoming energy and frequency into a single photon at twice the frequency, $\chi^{(2)}$ is the coefficient for only highly organized non-centrocymmetric molecule, $E(\omega)$ is the laser field amplitude, and $P^{NL}(2\omega)$ is the polarization.

$$P^{NL}(2\omega) = \frac{1}{2}\varepsilon_0\chi^{(2)}(2\omega{:}\,\omega,\omega)E(\omega)E(\omega) \qquad (1)$$

Similarly, THG is generated based on

$$P^{NL}(3\omega) = \frac{1}{4}\varepsilon_0 \chi^{(3)}(3\omega:\omega,\omega,\omega)E(\omega)E(\omega)E(\omega) \quad (2)$$

In case of THG, the signal generated is proportional to the $\chi^{(3)}(3\omega:\omega,\omega,\omega)$ tensor and unlike SHG, all materials have a non-vanishing $\chi^{(3)}$coefficient, which varies according to material properties and wavelength. According to the equations above, the generated HG intensity depends on the square (SHG) and cube (THG) of the incident light intensity. Similar to MEF, HG provides high spatial resolution and signal to noise ratio due to its quadratic and cubic dependencies on incident intensities [5].

2.1.3 Multi-Photon Microscopy

To increase the nonlinearly generated signal, it is important to use laser source that generates high peak power pulses. One advantage of multiphoton microscopy is that many fluorophores possess broad multi-photon excitation spectra [6]. In other words, several fluorophores and even harmonic generation can be excited at the same time with the same laser source if laser is set at a wavelength that covers the multi-photon cross section of all nonlinear events.

Multi-photon microscopy is designed to deliver laser pulse into highly scattering biological tissue and efficient signal collection. First, beam size is adjusted through scan lens and tube lens so that the beam can fully cover the back aperture of the microscope objective. High NA objectives spatially focus pulsed-laser photons to generates MEF and/or HG at the focus, which travels back through the same objective. Emission signal from the specimen then gets routed to detection optics by a long pass primary dichroic which reflects shorter wavelength signals. Additional dichroic mirrors are required to spectrally separate emitted light into multiple channels. Light separated by dichroic

mirrors is further filtered by a band pass filter to select for a more narrow wavelength range and then gets detected onto a photomultiplier tube (PMT). PMT signals are digitally converted and arranged into an imaging frame. A schematic of the multi-photon microscope used to acquire data presented in this thesis is shown in Figure 2.1.

2.2 Laser Ablation

Another application of nonlinear optics is to physically manipulate an biological material by multi-photon ionization [7]. Just like in MEF, multiple photons can be absorbed from a tightly focused intense pulse of laser light and excite electrons from the valence band into the conduction band. The energy applied here should be equal to or greater than the band-gap minimum of the material of interest.

When laser intensity at the focus is sufficiently high, the electron in the conduction band can be elevated to an even higher state. This electron can then collide with electron in the valence band and transfer some of its energy so that both electrons can stay in the conduction band (donor electron must have energy greater than the band-gap minimum). Following the initial ionization, a series of ionization events can follow until all energy around is depleted. This cumulative ionization process is called avalanche ionization. Ionization leads to a high-density electron-ion plasma. This is followed by a pressure wave and a cavitation bubble that can damage a material in addition to the effects of ionization. With precise tuning of laser pulse energy and focusing through a microscope objective, the size of cavitation bubble can be confined at the focal point. The degree and size of femtosecond laser induced damage can be controlled through choosing focusing energy and number of pulses.

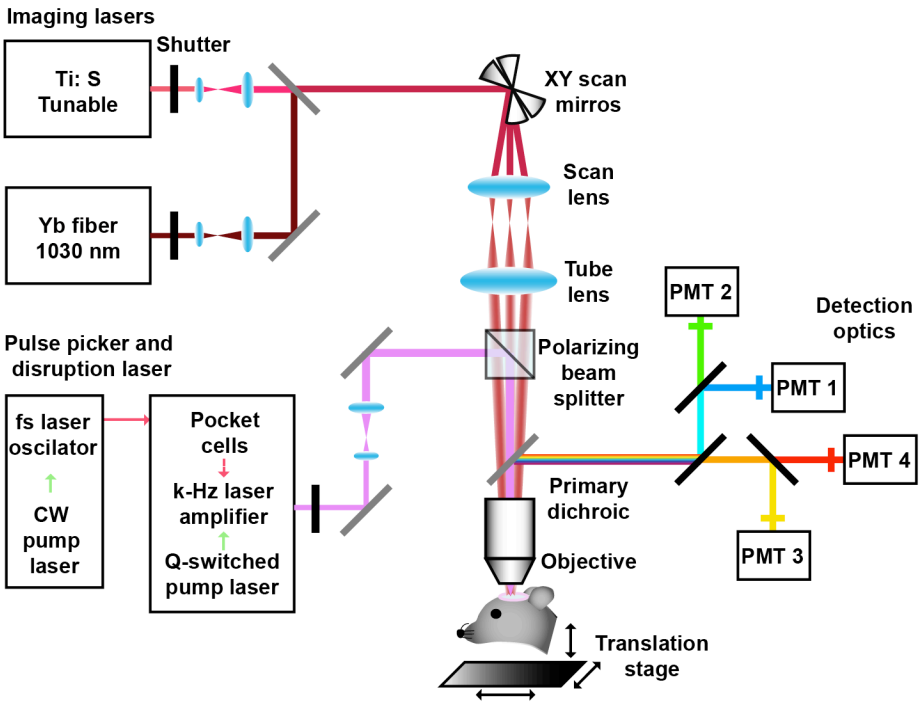

Figure 2.1 Schematic of four channel multi-photon microscopy equipped with femtosecond laser ablation

The work presented in this thesis utilized this laser-induced ionization to create small hemorrhages of cortical blood vessels in vivo [8]. Combined with multi-photon microscopy with four detection channels, we were able to study the response of multiple cellular populations to small bleeds in the brain. The ablation laser was collinearly aligned with the laser used for multiphoton microscopy after galvanometric scanners so that the ablation is fixed at relative to the induced imaging raster scan. This experimental setting allowed us to both induce and visualize the expansion of a hematoma as it was created.

REFERENCES

[1] W. R. Zipfel, R. M. Williams, and W. W. Webb, "Nonlinear magic: multiphoton microscopy in the biosciences," *Nat Biotech,* vol. 21, pp. 1369-1377, 11//print 2003.

[2] W. Denk, J. H. Strickler, and W. W. Webb, "Two-photon laser scanning microscopy," *Science,* vol. 248, 1990.

[3] N. G. Horton and C. Xu, "Dispersion compensation in three-photon fluorescence microscopy at 1,700 nm," *Biomedical Optics Express,* vol. 6, pp. 1392-1397, 2015/04/01 2015.

[4] W. R. Zipfel, "Live tissue intrinsic emission microscopy using multiphoton-excited native fluorescence and second harmonic generation," *Proc. Natl. Acad. Sci. USA,* vol. 100, pp. 7075-7080, // 2003.

[5] C.-K. Sun, S.-W. Chu, S.-Y. Chen, T.-H. Tsai, T.-M. Liu, C.-Y. Lin*, et al.*, "Higher harmonic generation microscopy for developmental biology," *Journal of Structural Biology,* vol. 147, pp. 19-30, 2004/07/01/ 2004.

[6] C. Xu and W. W. Webb, "Measurement of two-photon excitation cross sections of molecular fluorophores with data from 690 to 1050 nm," *Journal of the Optical Society of America B,* vol. 13, pp. 481-491, 1996/03/01 1996.

[7] B. S. Chris, B. André, and M. Eric, "Laser-induced breakdown and damage in bulk transparent materials induced by tightly focused femtosecond laser pulses," *Measurement Science and Technology,* vol. 12, p. 1784, 2001.

[8] N. Nishimura, C. B. Schaffer, B. Friedman, P. S. Tsai, P. D. Lyden, and D. Kleinfeld, "Targeted insult to subsurface cortical blood vessels using ultrashort laser pulses: three models of stroke," *Nature Methods,* vol. 3, pp. 99-108, Feb 2006.

CHAPTER THREE

CEREBRAL MICROHEMORRHAGES

3.1 Cerebral Microhemorrhages

Cerebral microhemorrhages or cortical microbleeds (CMBs) are small, up to 10mm in diameter, hemorrhagic strokes found in the brain. CMBs are often called as silent strokes since they don't illicit noticeable acute symptoms. These small injuries are mostly due to bleeding from small arterioles and capillaries. The development of various imaging modalities lead to increasing detections of CMBs are detected. Clinical studies have shown that aging and hypertension significantly increases the chance of such bleedings, and the National Institute of Health recognizes CMBs as a major factor in Alzheimer disease (AD) pathology. CMBs are also a risk factor for subsequent larger intracerebral hemorrhages, ischemic stroke, Binswager's disease, and AD. Therefore, more research needs to be done in both clinics and basic research settings to understand the pathophysiology of CMBs.

3.1.1 Diagnosis

In clinical practice, primarily to exclude hemorrhage and other pathologies such as brain tumors, computed tomography (CT) is primarily performed. CT can effectively show early signs of ischemia (e.g., swelling, changes in vessel density) and previous stroke lesions. However, magnetic resonance imaging (MRI) is preferred to CT for research and routine clinical use for screening since MRI features higher sensitivity and specificity for detecting pathological changes [1]. CMBs can be detected on a conventional MRI at 1.5T or 3T (higher the better) in T1- and T2-weighted spin echo images, but most are evident on T2*- weighted gradient recalled echo (GRE). CMBs appear as small round or ovoid homogeneous foci of black or hypointensity (ie, signal voids) on T2*-weighted GRE [2,

3]. After extravasation of erythrocytes into the parenchyma, various inflammatory responses degrade hemoglobin in erythrocytes and form hemosiderin, which is paramagnetic. Therefore, CMBs are effectively detected with MRI sequence susceptibility-weighted imaging (SWI), which is highly sensitive in detecting blood products, through the distortion of magnetic fields by calcium and hemosiderin deposits. CMBs are classified using a variety of size cut-off points with a maximum diameter of 5–10 mm and a minimum diameter of 2 mm, since the size of a CMB shown on MRI critically depends on imaging parameters, such as field strength and sequence [4]. In a clinical setting, this upper size limit is used to distinct CMBs from larger bleeds (macrobleeds). In a small number of studies that compared imaging and pathology, near-microscopic (<1–2 mm diameter) clusters of perivascular hemosiderin-laden macrophages were found around small perforating vessels in the histological counterparts of MRI imaging [5]. Other feasible pathologies that generate similar MRI signals are old hematomas, intact erythrocytes and, vascular pseudocalcification, microaneurysm, and distended dissected vessels [6]. These MRI detectable bleeds can be seen in up to 65% of patients diagnosed with vascular dementia [7]. Further advances in high-resolution novel imaging methods and clinical studies with extensive follow-up MRI scans will provide better understanding of the clinical consequences and the pathogenesis of currently under diagnosed CMBs.

3.2 Clinical Significance

3.2.1 Epidemiology and Risk Factors

Age is the most significant and independent risk factor for CMBs, with the prevalence gradually increase with age [8, 9]. Approximately half of the populations diagnosed with CMBs present multiple incidents [10]. Across multiple studies, the prevalence of CMBs in the elderly patients ranges between 24%~56% [8, 10-12]. Cardiovascular risk factors (ie, high systolic blood pressure, hypertension, smoking) and presence of cardiovascular disease are also linked to the presence of CMBs [8]. Lacunar ischemic stroke and patients with intracranial hemorrhages also present high incidence of small bleeds [13]. About half of the individuals suffering cerebral autosomal-dominant arteriopathy (CADASIL) with subcortical infarcts and leukoencephalopathy, caused by mutations of the Notch-3 gene also have CMBs [14]. Interestingly apolipoprotein (ApoE) $\varepsilon 4$ carriers are reported to have lobular CMBs in both younger and older population [8, 15]. Patients under anticoagulants and antithrombotic drugs have also reported higher incidence of CMBs [16]. CMBs detection is expected to further increase due to the rapid development and increasing availability of imaging methods.

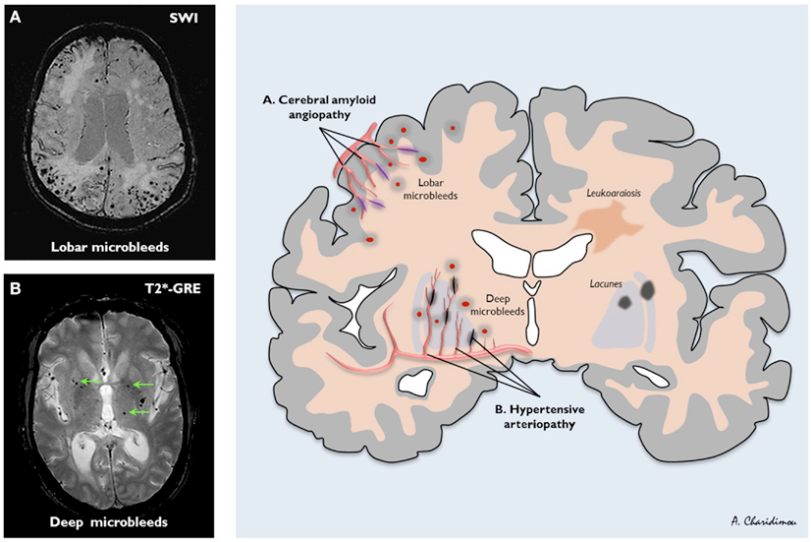

Figure 3.1 Distribution and the topography of cerebral microbleeds (CMBs). (figure from [17] used under Creative Common Attribution (CC BY version 4.0))

Cerebral amyloid angiopathy (CAA) and hypertension are the two major disease phenotypes directly linked to cause CMBs (Figure 3.1). Vessel stiffening due to CAA is known to correlate with cortical/subcortical lobar CMBs in CAA patients [18]. Hypertension is a major risk factor for CMBs and correlates with incidence in the elderly [9, 15, 19]. Where CMBs are located reflects the underlying small vessel disease. Strictly lobar CMBs are related to bleeding ensued from CAA pathology, while deep CMBs are due to hypertensive arteriopathy (Figure 3.1) [20-22]. CMBs due to hypertensive arteriopathy are also extensively found in the elderly.

CMBs are thought as the asymptomatic predecessor of symptomatic intracerebral hemorrhage (ICH), with the assumption that they may precede following traumatic stroke [18, 23]. This view hypothesizes that CMBs are already present at one's midlife and then slowly progress into a symptomatic ICH. Considering that hypertension develops over an asymptomatic period of decades, early detection of CMBs joined with clinically preventive care on both hypertensive and amyloid angiopathy can reduce the chance of traumatic ICH. In addition to cerebrovascular disease, CMBs also underlie neurodegenerative disorders, including AD and subcortical vascular dementia.

3.2.2 Mild cognitive decline

A faster progression of cognitive decline is found in patients with CMBs [10, 11, 24-27]. Cross-sectional analysis of the cognitive consequences of CMBs showed that the presence of CMBs is associated with impaired decision-making, decreased attention and processing speed, and decline of global cognition [13]. In a meta analysis based on

cognitive measurement between patients with and without CMBs, an significant trend of poor cognitive function was found (Figure 3.2). The behavioral severity of CMBs likely depends on multiple factors, including location, number, and size of CMBs and the presence of other diseases [25, 26]. To measure the distribution and prevalence of CMBs for quantitative diagnosis and disease categorization, a scale that includes the presence, number, and anatomical distribution called Microbleed Anatomical Rating Scale (MARS) is used [16, 27]. Which cognitive functions are perturbed depends mainly on the location of the CMBs. Generally, CMBs in deep brain regions, basal ganglia and thalamus, are associated with significant cognitive impairment [26]. CMBs found in the temporal lobe were associated with memory and attention impairment, whereas those found in the frontal lobe impairs memory, attention concept shifting, and psychomotor speed [25].

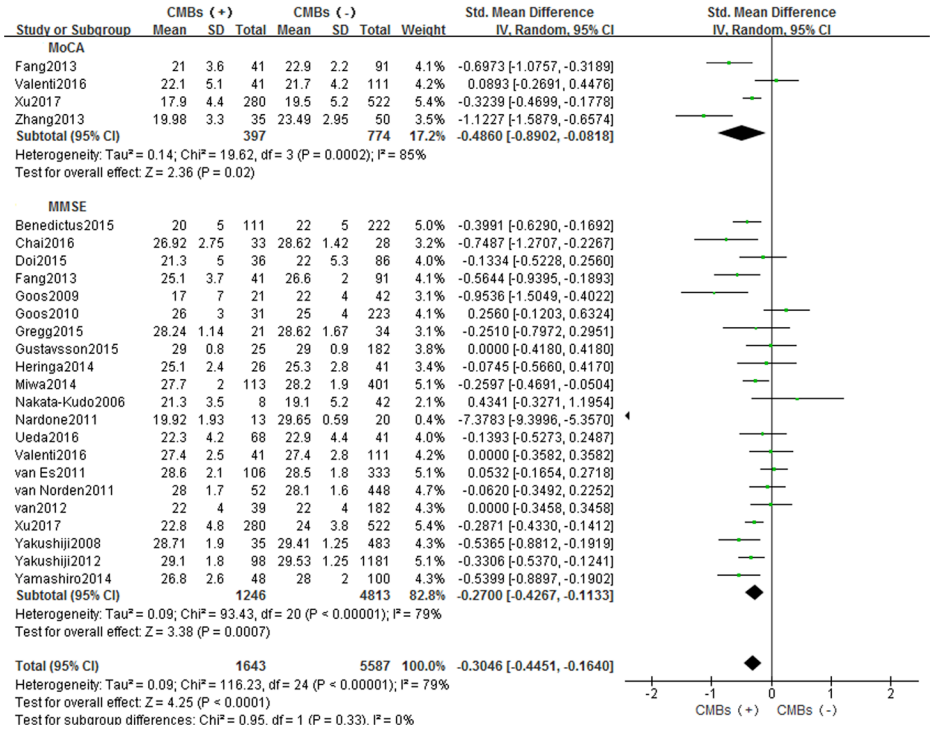

Figure 3.2 Meta-analysis of cognitive assessment score in CMBs versus non-CMBs. (figure from [28] used under Creative Common Attribution 4.0 International (CC BY 4.0))

The underlying mechanism by which CMBs cause cognitive decline is largely unknown. CMBs themselves may have direct effects by disrupting structural or functional connectivity of adjacent neurons, or if located at the junction, can reduce cortical–subcortical connections. In an animal study, microhemorrhages are known to cause a persisting local inflammatory response including activation of microglia and perivascular macrophages [28]. It is speculated that physical and chemical glial-neuron interaction may underlie the cellular basis of cognitive impairments in the neighboring brain region. A recent study proposed that multiple CMBs lead to disruption of structural networks in the brain [29]. However, studies have so far failed to demonstrate a clear association between CMBs and cognitive impairment mainly because the scope of the damage is quite limited and often the methodology of measuring cognition is not sensitive enough to catch subtle changes.

3.2.3 Subsequent Stroke and Mortality

A significant association between CMBs and subsequent symptomatic larger stroke is predicted in a number of studies. Clinical studies with consecutive brain MRI reveled a higher chance of getting ICH in elderly patients [3], and bigger intracerebral bleeding in patients with ischemic stroke with CMBs [30, 31]. AD patients with CMBs and patients receiving anticoagulants are also prone to cardiovascular events and stroke-associated mortality [32, 33]. This traumatic stroke may share similar causation with CMBs. In the Rotterdam study, the prospective population based study of the elderly followed up patients with CMBs up to 5 years have found strong correlation between mortality and non-CAA associated hypertensive CMBs [34]. Therefore, the presence of CMBs can be

an important precedent for larger stroke and traumatic cardiovascular diseases. Early detection of CMBs and following preventive treatments can therefore become a preventive routine of cardiovascular disease and traumatic larger stroke in near future.

3.2.4 Neuropsychiatric Symptoms

A number of neuropsychiatric symptoms are associated to the presence of CMBs. It is known that lobar CMBs are indicators for risk and progression of post-stroke depression [35]. Lobar CMBs and subcortical CMBs are associated with developing suicidality and fatigue, respectively [36, 37]. CMBs might serve as a pathological mechanism underlying emotional liability. Emotional incontinence, such as emotional disinhibition, has been found to associate with CMBs [38]. Behavioral and emotional disinhibition is also commonly found in patients with AD and its severity increases as the disease progresses [39]. Since CAA is a phenotype of AD, CMBs and AD may share similar mechanisms. These neuropsychiatric symptoms could be due to disorders in neural circuitry, such as molecular mechanisms and perturbed neurotransmission [40].

3.3 Pathophysiology

Although almost all vascular risk factors and other pathophysiological conditions in the brain are known to be associated with CMBs, the cellular and molecular mechanism underlying how CMBs develop is unknown. Hypertension is the most common risk factor of CMBs, but other genetic and environmental factors contribute. Therefore, in this part of the chapter, age-related degeneration of vascular components and functional maladaptation to blood flow maintenance is reviewed.

3.3.1 Molecular and Cellular Determinants

Alteration in the extracellular matrix of various tissues that make up vessels in the brain can lead to CMBs. The tensile strength of the vascular wall is greatly determined by collagen and elastin deposited around smooth muscle cells. Collagen fibers in cerebral arterioles are known to prevent damage to the elastic components of the vascular wall. Therefore, degenerative or inflammatory changes affecting walls of small arterioles cause structural weakening and eventually rupture of the vascular wall. Disruption of the extracellular matrix is also a well-understood factor in developing CMBs. Significant elastin degradation is found in CAA patients. Patients with genetic disorders affecting components of the extracellular matrix often present with micro to macro scale intracerebral hemorrhages [41]. One widely used research animal model of intracerebral hemorrhage uses the injection of extracellular matrix-degrading enzymes such as elastase and collagenases into the brain tissue [42].

In response to hypertension, vascular smooth muscle cells sense the increase in wall tensile stress. In healthy young organisms, smooth muscle cells attenuate mechanical stress within the vascular wall and reduce susceptibility for rupture. However, under pathological conditions or in aging, this mechanical adaptation processes does not function appropriately and intracerebral hemorrhages/CMBs occur. Smooth muscle cell loss is common in vessels affected by CAA [43] and decreased cross sectional area of smooth muscle cell is found in cerebral arterioles of elderly [44]. Smooth muscle atrophy in cerebral arterioles increases susceptibility for vessel rupture. Histological findings

from both human patients affected by CADASIL and animal models of CADASIL suggest the primary pathology is related to CMBs is the gradual degeneration of smooth muscle cells and consequential structure weakening of cerebral vessel [45, 46].

3.3.2 Increased pulse pressure on the brain microvasculature

The Windkessel effect refers to the shape of the arterial blood pressure waveform formed by the interrelation of the cardiac stroke volume and the compliance of the aorta and large elastic arteries. It involves an elastic reservoir in large arteries caused by mismatch of blood flow between large cardiac output and relatively smaller volume of blood leaving arteries due to the peripheral resistance. Arteries that display the Windkessel effect store blood during systole and constantly discharge during both systole and diastole. The fluctuation of blood pressure throughout cardiac cycle thus can be dampened and allow consistent perfusion to other organs in the body. Myogenic responses in healthy individuals involve powerful constraint against cardiac pressure in small cerebral arteries that significantly increases hydrodynamic resistance. Due to a large pressure drop along the resistance arteries, transmission of transient or chronic surges in pulsatile pressure is prevented from reaching the distal brain microcirculation. Both age-related process and exposure to vascular risk factors in the elderly increase aortic stiffness. Aortic Windkessel compliance is often impaired, and pulsatile systolic pressure transients travel without substantial attenuation within the cerebral circulation and reach the vulnerable portion of the microvasculature, exacerbating microvascular damage [47]. Microvascular injury in the brain has been hypothesized to result from increased pulsatile pressure having adverse effect on thinned aging microvasculature [5, 48]. Clinical and

experimental evidence suggests that the presence of pulsatile blood flow in elderly population leads to pressure-induced microvascular injuries [47, 49, 50]. Taken together, age-related autoregulatory dysfunction can be an important contributing factor to the pathogenesis of CMBs, and other microvascular injury that lead to blood brain barrier disruption, neuroinflammation, and white matter disease.

REFERENCE

[1] M. Brainin, J. Tuomilehto, W. D. Heiss, N. M. Bornstein, P. M. Bath, Y. Teuschl*, et al.*, "Post-stroke cognitive decline: an update and perspectives for clinical research," *Eur J Neurol,* vol. 22, pp. 229-38, e13-6, Feb 2015.

[2] H. C. Koennecke, "Cerebral microbleeds on MRI: prevalence, associations, and potential clinical implications," *Neurology,* vol. 66, pp. 165-71, Jan 24 2006.

[3] Y. Tsushima, J. Aoki, and K. Endo, "Brain Microhemorrhages Detected on T2*-Weighted Gradient-Echo MR Images," *American Journal of Neuroradiology,* vol. 24, pp. 88-96, 2003.

[4] C. Cordonnier, R. Al-Shahi Salman, and J. Wardlaw, "Spontaneous brain microbleeds: systematic review, subgroup analyses and standards for study design and reporting," *Brain,* vol. 130, pp. 1988-2003, Aug 2007.

[5] Y. Shi and J. M. Wardlaw, "Update on cerebral small vessel disease: a dynamic whole-brain disease," *Stroke and Vascular Neurology,* 2016.

[6] A. Shoamanesh, C. S. Kwok, and O. Benavente, "Cerebral microbleeds: histopathological correlation of neuroimaging," *Cerebrovasc Dis,* vol. 32, pp. 528-34, 2011.

[7] C. Cordonnier, W. M. van der Flier, J. D. Sluimer, D. Leys, F. Barkhof, and P. Scheltens, "Prevalence and severity of microbleeds in a memory clinic setting," *Neurology,* vol. 66, pp. 1356-60, May 09 2006.

[8] M. M. Poels, M. W. Vernooij, M. A. Ikram, A. Hofman, G. P. Krestin, A. van der Lugt*, et al.*, "Prevalence and risk factors of cerebral microbleeds: an update of the Rotterdam scan study," *Stroke,* vol. 41, pp. S103-6, Oct 2010.

[9] J. R. Romero, S. R. Preis, A. Beiser, C. DeCarli, A. Viswanathan, S. Martinez-Ramirez*, et al.*, "Risk factors, stroke prevention treatments, and prevalence of cerebral microbleeds in the Framingham Heart Study," *Stroke,* vol. 45, pp. 1492-4, May 2014.

[10] S. Hilal, M. Saini, C. S. Tan, J. A. Catindig, W. I. Koay, W. J. Niessen*, et al.*, "Cerebral microbleeds and cognition: the epidemiology of dementia in Singapore study," *Alzheimer Dis Assoc Disord,* vol. 28, pp. 106-12, Apr-Jun 2014.

[11] M. M. F. Poels, M. A. Ikram, A. van der Lugt, A. Hofman, W. J. Niessen, G. P. Krestin*, et al.*, "Cerebral microbleeds are associated with worse cognitive function The Rotterdam Scan Study," *Neurology,* vol. 78, pp. 326-333, Jan 2012.

[12] A. F. Wiegman, I. B. Meier, N. Schupf, J. J. Manly, V. A. Guzman, A. Narkhede*, et al.*, "Cerebral microbleeds in a multiethnic elderly community: demographic and clinical correlates," *J Neurol Sci,* vol. 345, pp. 125-30, Oct 15 2014.

[13] P. A. Yates, V. L. Villemagne, K. A. Ellis, P. M. Desmond, C. L. Masters, and C. C. Rowe, "Cerebral microbleeds: a review of clinical, genetic, and neuroimaging associations," *Front Neurol,* vol. 4, p. 205, Jan 06 2014.

[14] R. van den Boom, S. A. Lesnik Oberstein, M. D. Ferrari, J. Haan, and M. A. van Buchem, "Cerebral autosomal dominant arteriopathy with subcortical infarcts and leukoencephalopathy: MR imaging findings at different ages--3rd-6th decades," *Radiology,* vol. 229, pp. 683-90, Dec 2003.

[15] S. Sveinbjornsdottir, S. Sigurdsson, T. Aspelund, O. Kjartansson, G. Eiriksdottir, B. Valtysdottir*, et al.*, "Cerebral microbleeds in the population based AGES-Reykjavik study: prevalence and location," *J Neurol Neurosurg Psychiatry,* vol. 79, pp. 1002-6, Sep 2008.

[16] P. Kakar, A. Charidimou, and D. J. Werring, "Cerebral microbleeds: A new dilemma in stroke medicine," *JRSM Cardiovascular Disease,* vol. 1, pp. 1-14, 2012.

[17] A. Charidimou, C. Shakeshaft, and D. Werring, "Cerebral Microbleeds on Magnetic Resonance Imaging and Anticoagulant-Associated Intracerebral Hemorrhage Risk," *Frontiers in Neurology,* vol. 3, 2012-September-19 2012.

[18] H. V. Vinters and J. J. Gilbert, "Cerebral amyloid angiopathy: incidence and complications in the aging brain. II. The distribution of amyloid vascular changes," *Stroke,* vol. 14, pp. 924-8, Nov-Dec 1983.

[19] T. Jeerakathil, P. A. Wolf, A. Beiser, J. K. Hald, R. Au, C. S. Kase*, et al.*, "Cerebral microbleeds: prevalence and associations with cardiovascular risk factors in the Framingham Study," *Stroke,* vol. 35, pp. 1831-5, Aug 2004.

[20] S. M. Greenberg, M. W. Vernooij, C. Cordonnier, A. Viswanathan, R. Al-Shahi Salman, S. Warach*, et al.*, "Cerebral microbleeds: a guide to detection and interpretation," *Lancet Neurol,* vol. 8, pp. 165-74, Feb 2009.

[21] L. Pantoni, "Cerebral small vessel disease: from pathogenesis and clinical characteristics to therapeutic challenges," *Lancet Neurol,* vol. 9, pp. 689-701, Jul 2010.

[22] "Cerebral microbleeds: detection, mechanisms and clinical challenges," *Future Neurology,* vol. 6, pp. 587-611, 2011.

[23] A. Viswanathan and H. Chabriat, "Cerebral microhemorrhage," *Stroke,* vol. 37, pp. 550-5, Feb 2006.

[24] C. Chai, Z. Wang, L. Fan, M. Zhang, Z. Chu, C. Zuo*, et al.*, "Increased Number and Distribution of Cerebral Microbleeds Is a Risk Factor for Cognitive Dysfunction in Hemodialysis Patients: A Longitudinal Study," *Medicine (Baltimore),* vol. 95, p. e2974, Mar 2016.

[25] A. G. van Norden, H. A. van den Berg, K. F. de Laat, R. A. Gons, E. J. van Dijk, and F. E. de Leeuw, "Frontal and temporal microbleeds are related to cognitive function: the Radboud University Nijmegen Diffusion Tensor and Magnetic Resonance Cohort (RUN DMC) Study," *Stroke,* vol. 42, pp. 3382-6, Dec 2011.

[26] R. Wu, C. Feng, Y. Zhao, A. P. Jin, M. Fang, and X. Liu, "A meta-analysis of association between cerebral microbleeds and cognitive impairment," *Med Sci Monit,* vol. 20, pp. 2189-98, Nov 07 2014.

[27] S. M. Gregoire, U. J. Chaudhary, M. M. Brown, T. A. Yousry, C. Kallis, H. R. Jager*, et al.*, "The Microbleed Anatomical Rating Scale (MARS): reliability of a tool to map brain microbleeds," *Neurology,* vol. 73, pp. 1759-66, Nov 24 2009.

[28] X. Li, J. Yuan, L. Yang, W. Qin, S. Yang, Y. Li*, et al.*, "The significant effects of cerebral microbleeds on cognitive dysfunction: An updated meta-analysis," vol. 12, p. e0185145, 2017.

[29] N. L. Rosidi, J. Zhou, S. Pattanaik, P. Wang, W. Jin, M. Brophy*, et al.*, "Cortical microhemorrhages cause local inflammation but do not trigger widespread dendrite degeneration," *PLoS One,* vol. 6, p. e26612, 2011.

[30] S. M. Heringa, Y. D. Reijmer, A. Leemans, H. L. Koek, L. J. Kappelle, and G. J. Biessels, "Multiple microbleeds are related to cerebral network disruptions in patients with early Alzheimer's disease," *J Alzheimers Dis,* vol. 38, pp. 211-21, 2014.

[31] N. Nighoghossian, M. Hermier, P. Adeleine, K. Blanc-Lasserre, L. Derex, J. Honnorat*, et al.*, "Old Microbleeds Are a Potential Risk Factor for Cerebral Bleeding After Ischemic Stroke," *A Gradient-Echo T2*-Weighted Brain MRI Study,* vol. 33, pp. 735-742, 2002.

[32] Y. H. Fan, L. Zhang, W. W. M. Lam, V. C. T. Mok, and K. S. Wong, "Cerebral Microbleeds as a Risk Factor for Subsequent Intracerebral Hemorrhages Among Patients With Acute Ischemic Stroke," *Stroke,* vol. 34, pp. 2459-2462, 2003.

[33] M. R. Benedictus, N. D. Prins, J. D. Goos, P. Scheltens, F. Barkhof, and W. M. van der Flier, "Microbleeds, Mortality, and Stroke in Alzheimer Disease: The MISTRAL Study," *JAMA Neurol,* vol. 72, pp. 539-45, May 2015.

[34] C. E. Lovelock, C. Cordonnier, H. Naka, R. Al-Shahi Salman, C. L. M. Sudlow, T. Sorimachi*, et al.*, "Antithrombotic Drug Use, Cerebral Microbleeds, and Intracerebral Hemorrhage," *A Systematic Review of Published and Unpublished Studies,* vol. 41, pp. 1222-1228, 2010.

[35] S. Akoudad, M. L. Portegies, P. J. Koudstaal, A. Hofman, A. van der Lugt, M. A. Ikram*, et al.*, "Cerebral Microbleeds Are Associated With an Increased Risk of Stroke: The Rotterdam Study," *Circulation,* vol. 132, pp. 509-16, Aug 11 2015.

[36] W. K. Tang, Y. Chen, H. Liang, W. C. W. Chu, V. C. T. Mok, G. S. Ungvari*, et al.*, "Cerebral Microbleeds as a Predictor of 1-Year Outcome of Poststroke Depression," *Stroke,* vol. 45, pp. 77-81, 2014.

[37] W. K. Tang, Y. K. Chen, H. J. Liang, W. C. Chu, V. C. Mok, G. S. Ungvari*, et al.*, "Cerebral microbleeds and suicidality in stroke," *Psychosomatics,* vol. 53, pp. 439-45, Sep-Oct 2012.

[38] W. K. Tang, X. X. Liu, Y. K. Chen, J. Abrigo, W. C. Chu, V. C. Mok*, et al.*, "Cerebral microbleeds and fatigue in stroke," *Eur Neurol,* vol. 71, pp. 213-6, 2014.

[39] W. K. Tang, Y. K. Chen, J. Y. Lu, V. C. T. Mok, Y. T. Xiang, G. S. Ungvari*, et al.*, "Microbleeds and post-stroke emotional lability," *Journal of Neurology, Neurosurgery & Psychiatry,* vol. 80, pp. 1082-1086, 2009-10-01 00:00:00 2009.

[40] J. M. Ringman, L.-J. Liang, Y. Zhou, S. Vangala, E. Teng, S. Kremen*, et al.*, "Early behavioural changes in familial Alzheimer's disease in the Dominantly Inherited Alzheimer Network," *Brain,* vol. 138, pp. 1036-1045, 2015.

[41] D. Chaudhury, H. Liu, and M. H. Han, "Neuronal correlates of depression," *Cell Mol Life Sci,* vol. 72, pp. 4825-48, Dec 2015.

[42] O. M. Vanakker, D. Hemelsoet, and A. De Paepe, "Hereditary Connective Tissue Diseases in Young Adult Stroke: A Comprehensive Synthesis," *Stroke Research and Treatment,* vol. 2011, p. 712903, 01/20

[43] C. L. MacLellan, G. Silasi, A. M. Auriat, and F. Colbourne, "Rodent models of intracerebral hemorrhage," *Stroke,* vol. 41, pp. S95-8, Oct 2010.

[44] M. Merlini, D. Wanner, and R. M. Nitsch, "Tau pathology-dependent remodelling of cerebral arteries precedes Alzheimer's disease-related microvascular cerebral amyloid angiopathy," *Acta Neuropathol,* vol. 131, pp. 737-52, May 2016.

[45] X. Xu, B. Wang, C. Ren, J. Hu, D. A. Greenberg, T. Chen*, et al.*, "Age-related Impairment of Vascular Structure and Functions," *Aging Dis,* vol. 8, pp. 590-610, Oct 2017.

[46] P. Vitali, D. Boghen, N. Daneault, L. Guillon-Letourneau, and A. Y. Poppe, "Cerebral Microbleed Causing an Acute Stroke-like Episode in a CADASIL Patient," *Can J Neurol Sci,* vol. 41, pp. 661-3, Sep 2014.

[47] J. F. Arboleda-Velasquez, J. Manent, J. H. Lee, S. Tikka, C. Ospina, C. R. Vanderburg*, et al.*, "Hypomorphic Notch 3 alleles link Notch signaling to ischemic cerebral small-vessel disease," *Proc Natl Acad Sci U S A,* vol. 108, pp. E128-35, May 24 2011.

[48] T. Tarumi, M. Ayaz Khan, J. Liu, B. Y. Tseng, R. Parker, J. Riley*, et al.*, "Cerebral hemodynamics in normal aging: central artery stiffness, wave reflection, and pressure pulsatility," *J Cereb Blood Flow Metab,* vol. 34, pp. 971-8, Jun 2014.

[49] P. Soros, S. Whitehead, J. D. Spence, and V. Hachinski, "Antihypertensive treatment can prevent stroke and cognitive decline," *Nat Rev Neurol,* vol. 9, pp. 174-8, Mar 2013.

[50] F. M. Faraci and D. D. Heistad, "Regulation of large cerebral arteries and cerebral microvascular pressure," *Circ Res,* vol. 66, pp. 8-17, Jan 1990.

[51] T. P. Santisakultarm, N. R. Cornelius, N. Nishimura, A. I. Schafer, R. T. Silver, P. C. Doerschuk*, et al.*, "In vivo two-photon excited fluorescence microscopy reveals cardiac- and respiration-dependent pulsatile blood flow in cortical blood vessels in mice," *Am J Physiol Heart Circ Physiol,* vol. 302, pp. H1367-77, Apr 01 2012.

CHAPTER FOUR

CEREBRAL MICROHEMORRHAGES INDUCE A FOCAL, YET DIVERSIFIED INFLAMMATORY RESPONSE INCLUDING A COORDINATED PATTERN OF MICROGLIAL MIGRATION AND PROLIFERATION

4.1 Abstract

Due to advances in clinical imaging modalities, such as MRI, that enable the detection of cerebral microbleeds, the prevalence and impact of these lesions in the aging population has received increased emphasis. The presence of cerebral microbleeds is thought to gradually impair neuronal function and cause cognitive decline. Previous studies suggest that the reaction of inflammatory cells may play an important role in the physiological and cognitive impacts of cerebral microbleeds. However, due to its miniscule size and asymptomatic nature, on time detection and follow-up study of these small hemorrhages were impossible. Here, using extensive in vivo imaging through a cranial window implanted on adult mouse brain to follow up on the inflammatory responses after a femtosecond laser-induced cortical microhemorrhage, we found a diverse inflammatory responses including blood born leukocytes, brain resident microglia and astrocyte. We found that blood-borne leukocytes of different phenotypes invade over two weeks. We also found a concerted spatiotemporal pattern of microglia migration and proliferation near the injury. Proliferation was observed primarily in regions where migration decreased microglia density, suggesting that microglia sparsity can trigger focal proliferation. Albeit the small size, brain responds with a package of acute inflammatory responses to rearrange brain microenvironment that span up to two weeks.

4.2 Introduction

Compared to traumatic intracerebral hemorrhage cerebral microbleeds (CMBs) are common and occur at increasing frequency with age, hypertension, cerebral amyloid angiopathy, and with genetic conditions such as CADASIL [1]. CMBs vary in size from tens of micrometers to several millimeters, and while they are not associated with acute neurological symptoms there is growing evidence linking them to accelerated cognitive decline and to increased risk for dementia [1-3]. The cellular mechanisms by which CMBs affect the health and function of cells in the brain microenvironment remains poorly understood. We used a laser-based approach to induce CMBs from targeted arterioles in the cortical vasculature of mice. When targeting ~20-μm diameter penetrating arterioles, a reproducible ~150-μm diameter CMBs can be produced in the cortex [4-6] (Figure 4.1), comparable to the size of the smaller bleeds found in humans [7]. Using this model, we have previously reported that microhemorrhages do not lead to nearby cell death or degeneration of dendritic arbors [5], or to long-term loss of neural responsivity [6]. We did observe an increase in the density of inflammatory cells near the lesion, although the classes of cells involved and their origin were not determined [5]. Such inflammation could contribute to the cognitive decline associated with CMBs. Here, we use *in vivo* imaging to provide a comprehensive picture of the inflammatory response after a microhemorrhage, identifying the cell types involved, their spatiotemporal dynamics, and the mechanisms leading to increased inflammatory cell density near the lesion.

4.3 Results

To produce CMBs, we used a laser-based approach to rupture targeted penetrating arterioles, vessels that branch from the surface arteriole network and dive into the brain to feed capillary beds [6]. We irradiated the edge of the vessel lumen with short bursts of tightly-focused femtosecond laser pulses with sufficient energy to cause ionization of the material at the laser focus, causing the vessel wall to rupture and creating a hematoma of up to 150 μm in diameter (Figure 4.1). This laser irradiation deposited relatively little total energy, so there was minimal collateral damage to surrounding tissue from the laser itself. The ruptured wall of the targeted vessel clotted over a few seconds and restricted the size of the hematoma [5]. Blood flow in the targeted penetrating was not disrupted, so there is no ischemic injury in this model [4]. This model allows us to control the time and location of a CMB in the cortex, allowing the use of *in vivo* imaging to follow the cellular response to the injury. Here, we aim to identify the cellular players associated with the inflammatory response to a CMB. We used transgenic mouse lines and bone marrow transplant (BMT) chimeras to label different classes of inflammatory cells and study their role in the inflammatory response.

We first examined the role of blood-borne monocytes that invade the tissue after the injury. In wild-type mouse receiving bone marrow from $Cx3cr1^{GFP/+}$ mouse ($Cx3cr1^{GFP/+}$ → wild-type mice), primarily patrolling monocytes were labeled. We observed the infiltration of a small number of green fluorescent protein (GFP) positive cells over days to weeks after the lesion (Figure 4.2A top panel), which were nearly all in perivascular locations. In mice with inflammatory monocytes labeled with red fluorescent protein (RFP) ($Ccr2^{RFP/+}$), we observed the infiltration of a few labeled cells over a few days

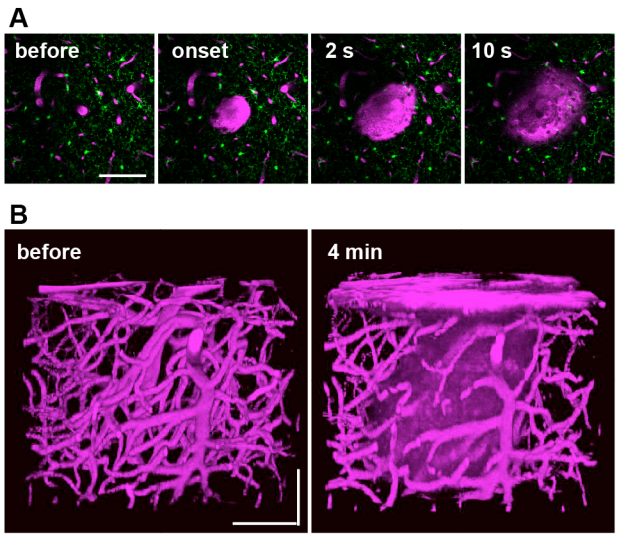

Figure 4.1 Femtosecond laser-induced cortical microhemorrhages (**A**) In vivo two-photon excited fluorescence images of fluorescently-labeled blood plasma (magenta, i.v. injected Texas Red dextran) during creation of a microhemorrhage by ablation of a cortical penetrating arteriole. (**B**) 3D reconstruction of the vasculature and extravagated plasma before and after the lesion.

after the lesion (Figure 4.2A middle panel), divided about equally between parenchymal and perivascular locations (Figure 4.2B). Finally, we imaged mice with all leukocytes labeled (UBC-GFP → wild-type), and, again, observed the infiltration of a small number of labeled cells (Figure 4.2A bottom panel), divided about equally between parenchymal and perivascular locations (Figure 4.2B). Small, punctate, autofluorescent spots also appeared over days after the lesion. To get away from irradiation triggered BBB damage, all irradiation for BMT were done with lead head shield that resulted in partial chimerism, which can represent a portion of cell of interest (All mice used in this experiment had more than 63% of bone marrow replaced). Taken together, these data suggest that a modest invasion of blood-borne cells occurs after a CMB, consisting of inflammatory monocytes (i.e. *Ccr2*$^{+}$) earlier and later patrolling monocytes (i.e. *Cx3cr1*$^{+}$). While there are only a few invading cells, the time course of the invasion of inflammatory and patrolling monocytes is similar to that seen after larger ischemic lesions, where blood-borne cells play a larger role [8].

We next determined the role of brain-resident microglia. As a kind of resident brain macrophage, microglia are the first cell type to respond to an inflammatory trigger in the central nervous system. Microglia are well known for their ability to surveil adjacent tissue by constantly extending and retracting their processes [9]. Without an injury, we saw no significant change in microglia location over weeks, although the spatial pattern made by their processes changed significantly (Supplementary fig. 4.1). However, in the presence of microhemorrhage, microglia extended processes toward the microhemorrhage within minutes (Supplementary fig. 4.1). In *Cx3cr1*$^{GFP/+}$ mice receiving

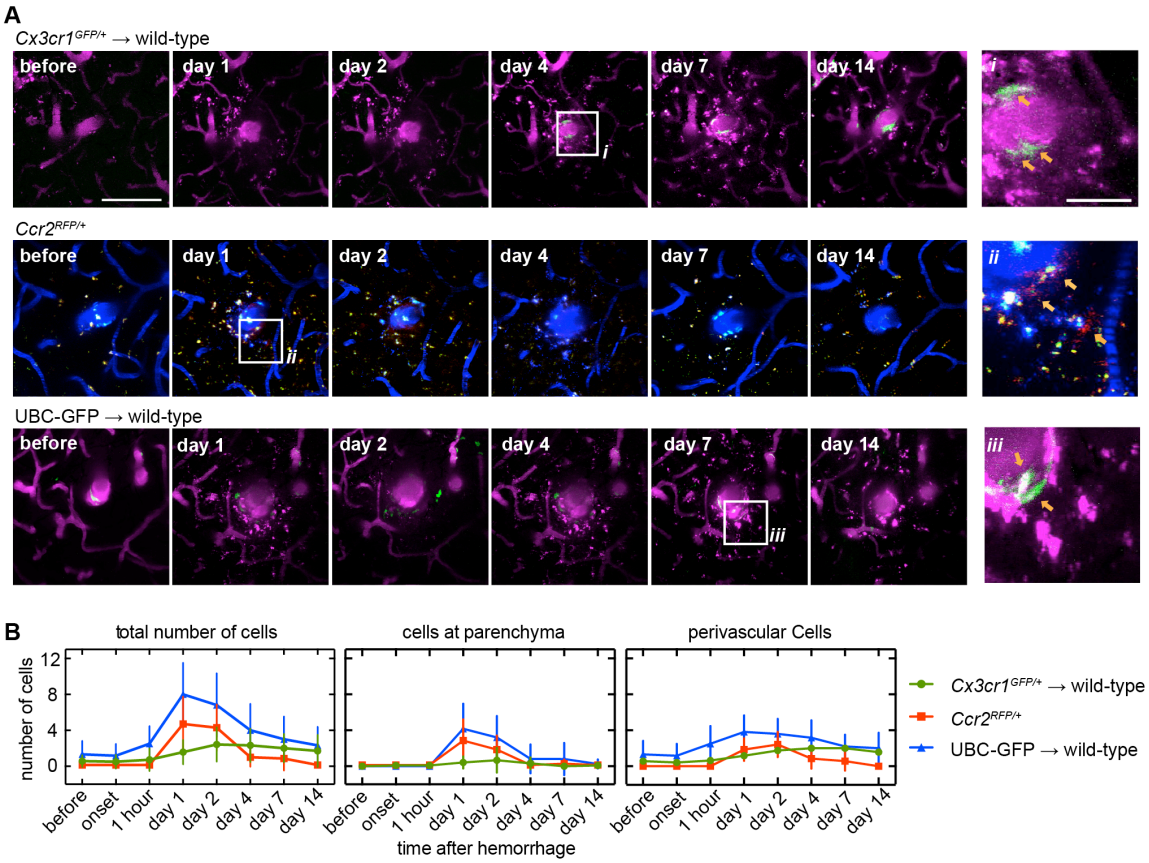

Figure 4.2 Invasion of a small number of blood-borne inflammatory cells (**A**) Axial projections image stacks showing the response of different genetically-labeled inflammatory cell types over 2 weeks after a microhemorrhage. In wild-type animals receiving a *Cx3cr1*$^{GFP/+}$ bone marrow transplant (*Cx3cr1*$^{GFP/+}$ → wild-type), labeled cells are patrolling monocytes (top panel, green, GFP). In *CCR2*$^{RFP/+}$ animals labeled cells are inflammatory monocytes (middle panel, red, RFP; blue, i.v. injected Cascade Blue dextran). In UBC → wild-type animals all circulating cells other than red blood cells are labeled (bottom panel, green, GFP). Location of insets (on right) are indicated with white boxes. (**B**) Number of cells within the image volume (230 X 230 X 40 µm, centered on microhemorrhage) over time for the same genetically-labeled cell populations show in A (left). The same data was broken down by cell location perivascular (defined as the cell touching the outside of the vessel; middle) and parenchymal (right) locations. (*Cx3cr1*$^{GFP/+}$ → wild-type: n=12 in 4; *CCR2*$^{RFP/+}$: n=6 in 3; UBC → wild-type: n=7 in 2). All scale bars are 100 µm, except for the insets in (A), which are 25 µm. Error bars indicate SD.

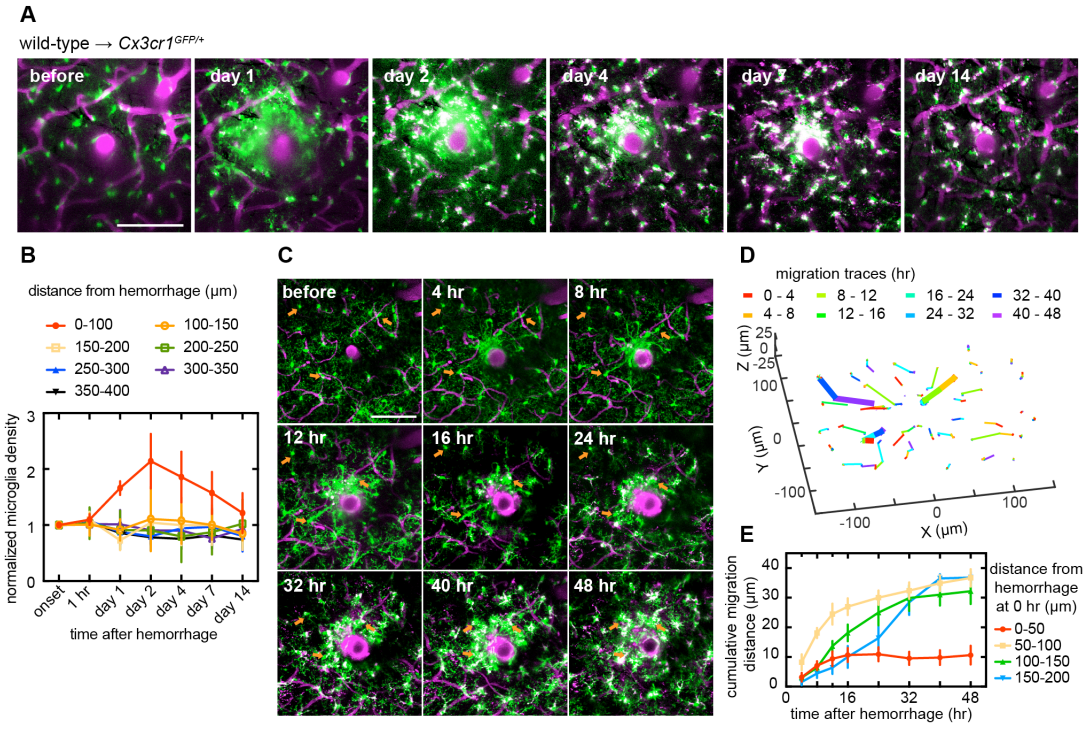

Figure 4.3 Local increase in microglia density was due to migration of nearby microglia toward the injury In *Cx3cr1*$^{GFP/+}$ animals receiving a wild-type bone marrow transplant (wild-type → *Cx3cr1*$^{GFP/+}$), labeled cells are nearly all microglia (green, GFP). Axial projections of two-photon image stacks showing the response microglia over 2 weeks after a microhemorrhage. (magenta, i.v. injected Texas Red dextran; green, GFP) (**B**) Plot of normalized density of microglia over time after a microhemorrhage for regions at different distance from the lesion (wild-type → *Cx3cr1*$^{GFP/+}$: n=5 hemorrhages from 3 mice). (**C**) Axial projections of 40-μm thick two photon image stacks over time after a microhemorrhage in a *Cx3cr1*$^{GFP/+}$ mouse. (**D**) Migration paths of the microglia from panel (C). The color of the segment indicates the time span when that migration occurred. The three bold paths correspond to the three cells identified with orange arrows in (C). (**E**) Cumulative radial migration distance between each time point toward the microhemorrhage for microglia with different initial distances from the target vessel (n=4 hemorrhages from 3 mice). All scale bars are 100 μm.

BMT from wild-type mice (wild-type → *Cx3cr1*$^{GFP/+}$) microglia were GFP labeled (as well as a fraction of patrolling monocytes due to incomplete chimerism). The density of GFP-labeled cells near the bleed increased over the first two days (Figure 4.3A). There was a trend toward decreased density of labeled cells at distances of 100-200 μm away from the injury at 1 day, which recovered by 2 days (Figure 4.3B). Microglia density near the lesion site then decreased over two weeks, with microglia regaining a more ramified morphology. We then determined the relative role of migration and proliferation in the microglia density increase near the microhemorrhage. We followed the movement of individual microglia over 48 hr after the lesion in *Cx3cr1*$^{GFP/+}$ mice (Figure 4.3C, D). Microglia migrated radially inward toward the lesion, with some cells traveling distances of up to 40 μm (Figure 4.3D). Microglia within 100 μm of the target vessel began to migrate within hours, while cells initially further from the lesion took progressively longer to begin migrating (Figure 4.3D). Migration speeds ranged from 0.5 – 2 μm/hour. In microglia that migrated, we observed a stereotypical temporal sequence where the cell first extended processes toward the lesion, then these processes became thicker, and finally the cell migrated along the path of the thickened process toward the lesion (Supplementary fig. 4.1). We also observed proliferation of some microglia using time-lapse 2PEF imaging at times 24 hours or later after the injury (Figure 4.4A, Supplementary fig. 4.2). To quantify the role of proliferation in the microglia density increase, we used 5-ethynyl-2'-deoxyuridine (EdU) labeling and immunohistology approaches (Figure 4.4B-D, Supplementary fig. 4.3). Interestingly, we found microglia proliferated predominantly in a ~100-μm wide shell with a ~175-μm radius that

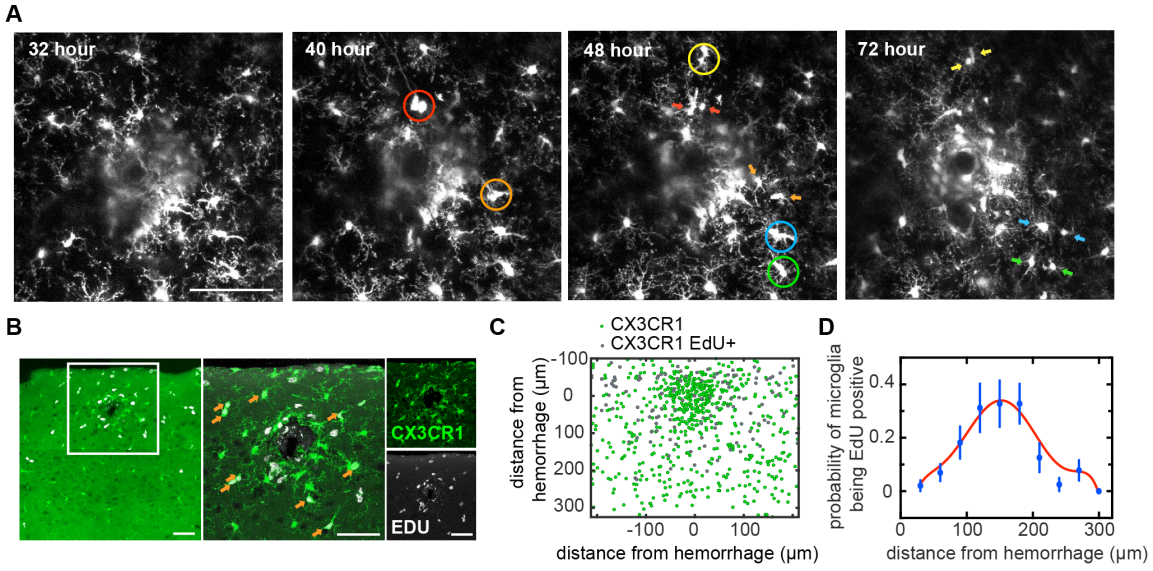

Figure 4.4 Proliferation of microglia was observed in a shell surrounding the lesion (**A**) Axial projections of 40-µm thick 2PEF image stacks over time after a microhemorrhage in a *Cx3cr1*$^{GFP/+}$ mouse. Colored circles indicate cells that will proliferate by the next time point. Arrows with matching colors indicate the pair of daughter cells. Scale bar is 100 µm. The full time series of this particular hemorrhage is shown in Supplementary figure 2. (**B**) Images of a coronal histological section that intersected a microhemorrhage from an animal sacrificed two days after the lesion and with repeated EdU injections. Cells that proliferated over those two days are labeled with EdU (white), while microglia are labeled with GFP (green). The white box in the left image indicates the region for the magnified images to the right. (**C**) Composite map of the location of all microglia and EdU+ microglia from coronal sections across 17 hemorrhages from three mice, with the location of the microhemorrhage centers aligned at (0,0). The cortical surface is at the top of the image. (**D**) The probability of microglia being EDU positive as a function of radial distance from the microhemorrhage from the data shown in (g) and a polynomial fit (red trend line). All scale bars are 100 µm.

surrounded the targeted penetrating arteriole (Figure 4.4C, D). Taken together, these data suggest that microglia near a microhemorrhage respond by rapidly migrating toward the injury, leading to a slight decrease in density in the surrounding neighborhood. After a day, microglia then proliferate in this region where the density had decreased. This pattern of migration and proliferation leads to increased density near the lesion while preserving microglia density farther away. After two days, the microglia density close to the injury began to slowly decline and neared baseline density by 2 weeks.

The spatial overlap between the regions of microglia density decrease and of microglia proliferation suggests that microglia may be triggered to proliferate when their local density decreases. To explore this idea, we computationally simulated the response of microglia to a microhemorrhage (Figure 4.5A). First, we used our experimental measurements to extract probability distributions for microglia migration distance (Supplementary figs. 4.4 and 4.5) and microglia proliferation (Figure 4.4D), each as a function of distance from and time after the microhemorrhage. The resulting simulations showed an increase in microglia density near the lesion over 48 hr that agreed with *in vivo* data, validating this simulation approach (Figure 4.5B). A surrounding shell-shaped region with a slightly decreased microglia density at 24 hr was also evident and filled in due to proliferation by 48 hr (Figure 4.5B). To test the idea that microglia proliferation depended on changes in the local microglia density, we next ran the simulation using experimentally measured microglia migration but now assuming that microglia were triggered to proliferate if their domain volume increased by more than a defined factor (Figure 4.5C and Supplementary fig. 4.6). We found that the simulation predicted the

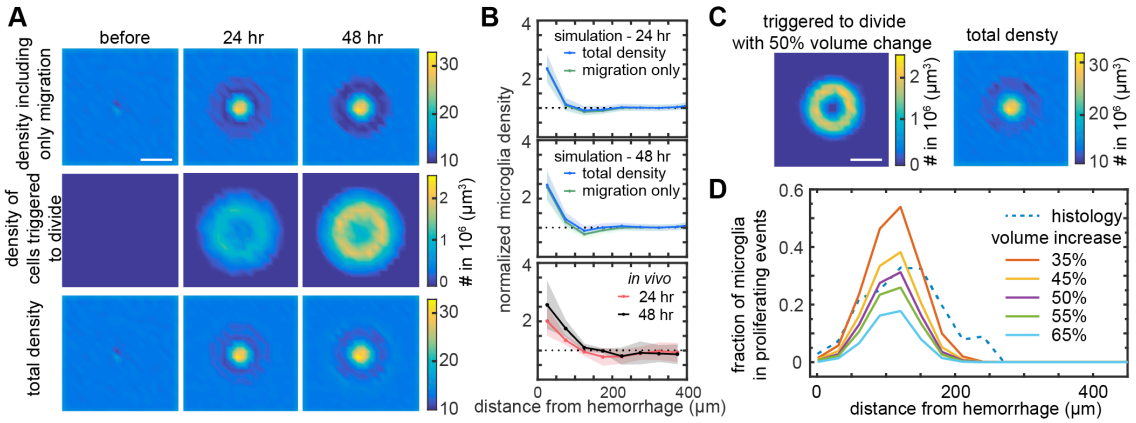

Figure 4.5 Simulation of microglia density changes due to migration and proliferation after a microhemorrhage (**A**) Map of the density of microglia including only migration and not proliferation in the simulation (top), of microglia committed to division (middle), and of total microglia density (bottom) at baseline and at 24 and 48 hrs after the microhemorrhage. (**B**) Plot of normalized density of microglia as a function of distance from a microhemorrhage at 24 (top) and 48 (middle) hrs after the injury for the simulation showing the density including migration and proliferation (blue) or just migration (green). The lower plot shows *in vivo* measurements at 24 (red) and 48 (black) hrs after the lesion (same data as shown in Figure 3B; n=5 hemorrhages from 3 mice). Lines (shading) indicate mean (SD). (**C**) Map of the total density of microglia (left) and of the density of microglia committed to division (right) at 48 hrs after a microhemorrhage using models where microglia proliferation occurs when the domain volume of a microglia increases by more than 50% percentage. (**D**) The fraction of microglia that have either committed to divide or are daughter cells of a proliferation event as a function of distance from and at 48 hrs after the microhemorrhage for different density-dependent microglia proliferation models. The dashed line represents the fraction of microglia that were found to be EdU positive in experiments (same data as in Fig. 4D). Scale bars are 200 μm.

observed spatial distribution of microglia proliferation using a 50% volume increase as the threshold value to trigger a proliferative event (Figure 4.5D).

We also sought to understand the participation of astrocytes in the inflammatory response following a CMB. Astrocytes are another subtype of glia cell having numerous functions including guiding neuronal development and synapse formation, facilitating proper propagation of action potentials, and acting as one of the gate keepers of the brain by being part of the brain blood barrier (BBB). Coordination between microglia and astrocytes seems required for fine-tuned regulation and resolution of inflammatory responses [10]. Although the representation of astrocyte reactivity by the expression level of glial fibrillary acidic protein (GFAP) is still debatable, this approach is widely used. After creating laser-induced microhemorrhages in *Cx3cr1*$^{GFP/+}$ mice, we sacrificed mice at different time points and immune-stained for GFAP. We saw extensive expression of GFAP around the lesion starting two days and peaking at seven days after the injury (Figure 4.6A). Over time, GFAP expression declined and an astrocytic glial scar was not found near the lesion at later time points (Figure 4.6B).

4.4 Discussion

Although CMBs do not elicit noticeable symptoms, increasing evidence suggests that CMBs are not clinically silent. CMBs are common in the elderly population and are more prevalent in patients with cardiovascular risk factors, such as hypertension. The presence of CMBs is highly correlated with cognitive impairment and functional decline. However, the underlying mechanism by which CMBs cause cognitive decline is largely

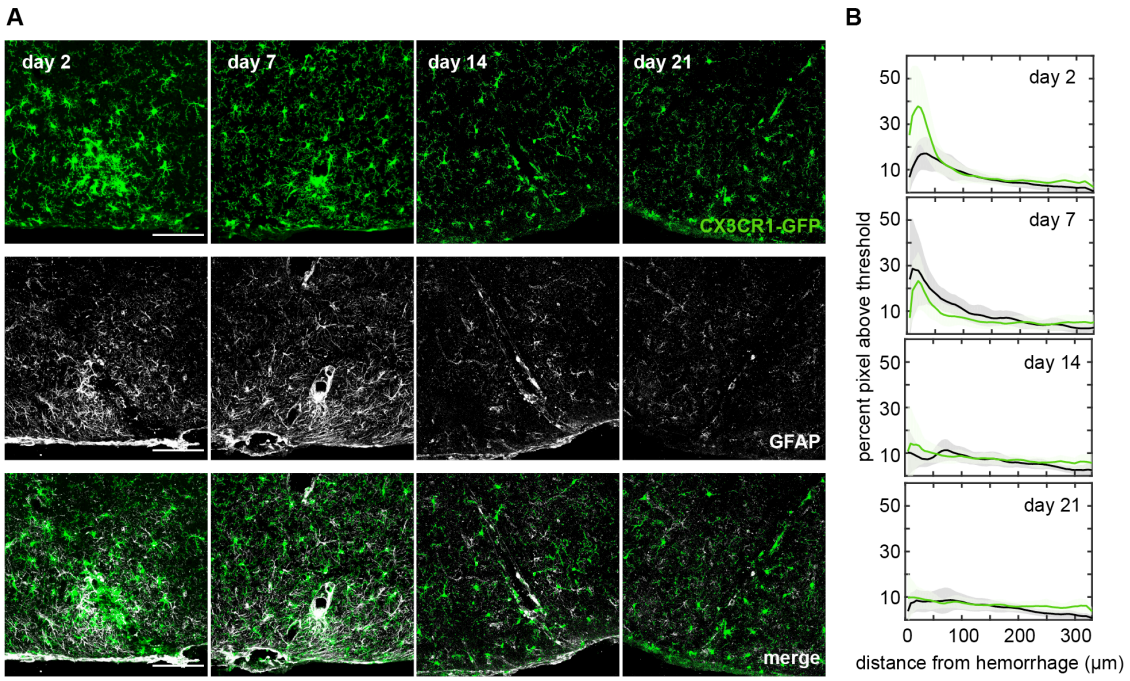

Figure 4.6 Dense appearance of astrocytes near the hemorrhage (A) Images of coronal histological section that intersected a microhemorrhage from animals sacrificed two, seven, fourteen, and twenty one days after the lesion. Microglia are visualized by the expression of CX3CR1-GFP (top panels), astrocytes are visualized by immunolabeling of GFAP (middle panels). The bottom panels show and overlay. (B) The number of image pixels above a threshold as a function of distance distance away from the lesion and over time for microglia and astrocytes. Scale bars are 100µm.

unknown. To understand how the brain responds to such small bleeds, we used a series of *in vivo* imaging to follow the behavior of a number of different cell types after the injury. In previous studies, we found that these bleeds to not cause the death of nearby neurons nor the degeneration of their dendritic arbors. We also found that while neurons near the injury initially fired fewer action potentials in response to a stimulus, they recovered within hours. In this work, we detail the cellular players in the inflammatory response we observe after the injury. The initial response was dominated by brain-resident microglia, which exhibited a coordinated pattern of migration and proliferation that led to an increased density of microglia near the lesion (primarily by migration from the surrounding tissue), while later recovering the density of microglia in the surrounding tissue (by proliferation). A small number of invading leukocytes were also observed, with more inflammatory monocytes earlier, followed by patrolling monocytes. Although the number of invading monocytes was small, these cells were present near the lesion for days, perhaps participating in regulating the inflammatory response with brain resident glial cells.

The concept of neuroinflammation implies an inflammatory process originate primarily from brain resident glial cells. Glial cells that primarily respond to inflammatory insults are microglia, the resident myeloid cells of the brain, as well as astrocytes. Both microglia and astrocytes have pro- and anti-inflammatory functions dependent on the mode of injury. In response to inflammatory stimuli, microglia take on a phagocytic phenotype to clear cellular debris, and secrete cytotoxic factors, cytokines, growth

factors, and even neurotransmitters that may influence function in neurons and other cells [11]. It is known that Interleukin-1β (IL-1β) levels increase during long term potentiation (LTP) and are required for maintenance of long term changes [12]. Increased release of IL-1β by microglia in normal conditions can thus have a mild effect on LTP signaling. Tumor necrosis factor-α (TNFα), also released by microglia, is involved in synaptic plasticity by increasing surface AMPA receptors [13]. Interestingly, mice deficient in CX3CR1/CX3CL1 (fractalkine receptor in microglia) are reported to lack LTP and hippocampal-dependent learning and memory, suggesting that microglia may play a key role in synaptic plasticity [14]. These actions by microglia can either exacerbate damage by, for example, promoting excitotoxic injury [15] or inappropriately phagocytosing synapses [16], or they may play a protective role by, for example, limiting neuronal injury due to ischemia [17]. Thus, activation and redistribution of microglia near a CMB likely affects the behavior of nearby neurons and other cells and may contribute to the cognitive effects associated with these lesions. The function of astrocytes was long thought to be restricted to maintaining and supporting the health and function of neurons. However, it is now widely understood that astrocytes actively respond in an array of CNS diseases, just like microglia. Recently, it has been found that microglia activation induces A1 reactive astrocyte by releasing three cytokines: Interleukin 1 alpha (IL-1α), TNFα, and the complement component subunit 1q (C1q) [18]. Reactive astrocytes can be more harmful than protective to the adjacent neuronal population. Altogether, coordinated activation of microglia and astrocyte can change the strength of synaptic connectivity, affect synapse formation, and participate in maturation and elimination of neuronal spines, all of which are the fundamental basis of neuronal plasticity.

In the healthy brain, microglia are intercalated throughout the entire parenchyma and are arranged in non-overlapping domains, which they surveil by extending and retracting processes [9]. Through this surveillance, microglia can detect subtle changes in the microenvironment and react to any kind of insult, sensed with an array of surface receptors including purigenic [19] and fractalkine [20] receptors, as well as receptors for complement fragments [21], immunoglobulin, and adhesion molecules [22]. Like other tissue-resident macrophages, microglia maintain their population locally by proliferative self-renewal [23-26], with sporadic proliferation under normal conditions and clonal expansion under pathological conditions [26]. Here, through a series of *in vivo* analyses, we describe the concerted spatiotemporal response of microglial migration and proliferation in a focal injury model. We observed proliferation of microglia predominantly in regions where the density of microglia declined due to migration, suggesting that microglia sense their local density and proliferate when the density decreases. It is not clear how microglia sense such changes in density, but it has been reported that microglial processes repel one another when they make contact [9]. This coordinated pattern of migration and proliferation can thus explain how microglia maintain their characteristic organization in non-overlapping domains after a nearby focal injury.

Here in this work, a single event of bleeding from a penetrating arteriole induced a series of microglia and later astrocyte activation as well as invasion of monocytes of different phenotype that spans more than a week. Although this small bleed does not cause direct

neuronal degeneration [5] nor loss of responsiveness to external stimuli [6], this prolonged inflammatory response could cause subtle modulation of normal brain function, and the accumulation of such events could in later life, underlie cognitive decline.

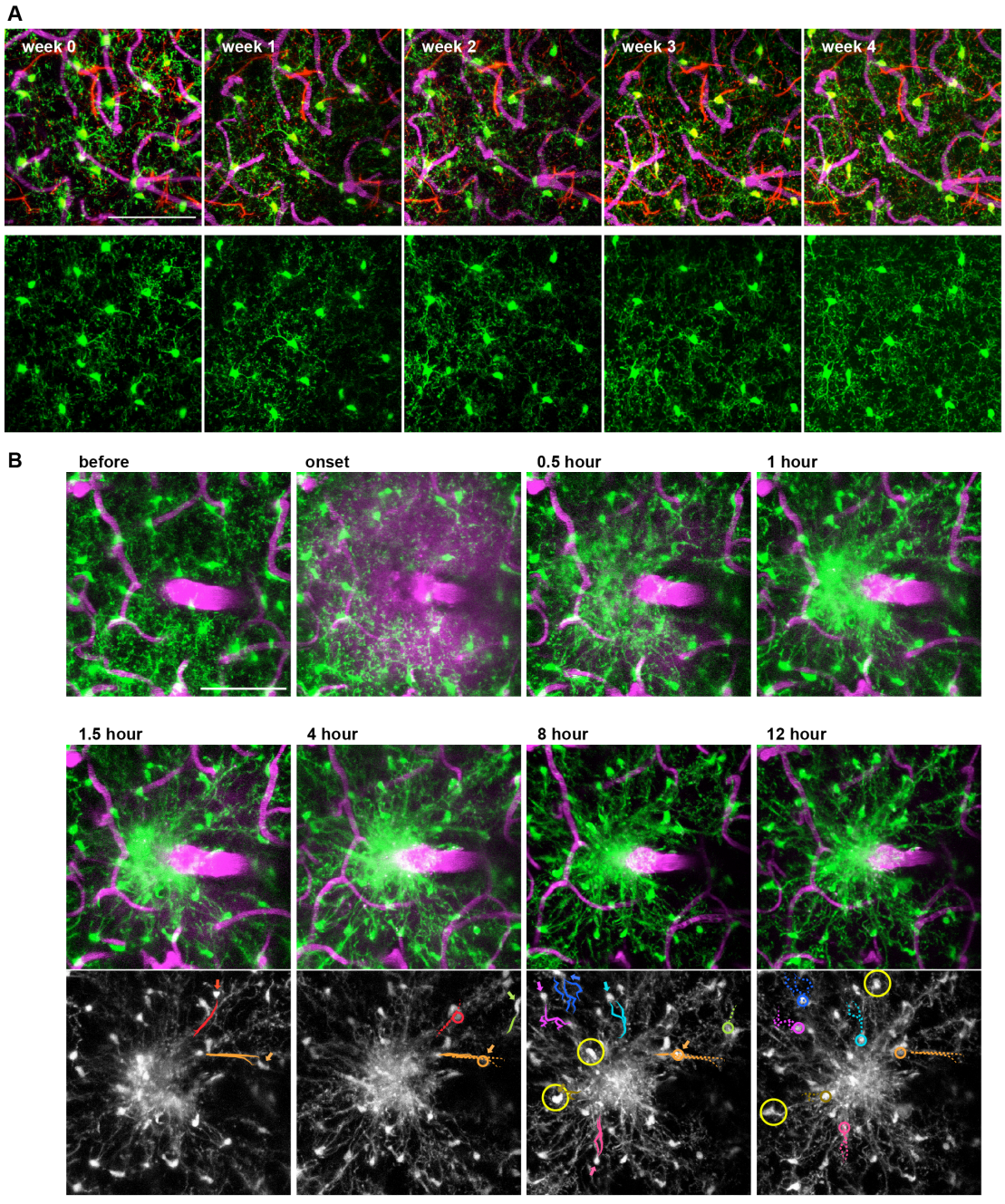
A
week 0
week 1
week 2
week 3
week 4
B
before
onset
0.5 hour
1 hour
1.5 hour
4 hour
8 hour
12 hour

Supplementary figure 4.1 Microglia locations were highly stable in the absence of an injury but immediately responded to a microhemorrhage and migrateed toward the injury following a path defined by previous processes extension (**A**) Axial projections of 50-µm thick 2PEF image stacks over time in a *Cx3cr1*$^{GFP/+}$ mouse taken ~100 µm beneath the cortical surface on the contralateral side of the brain from the location of any microhemorrhage (magenta, i.v. injected Texas Red dextran; green, GFP; red, YFP expressed in Layer V pyramidal neurons). Although the microglial processes differed in spatial arrangement between time points, nearly all microglia in the imaging field retained their approximate position. Scale bar is 50 µm. (**B**) Axial projections of 40-µm thick 2PEF image stacks over time after a microhemorrhage in a *Cx3cr1*$^{GFP/+}$ mouse (magenta, i.v. injected Texas Red dextran; green, GFP). The grey-scale images show just the GFP-labeled microglia for the last four time points. For several cells, the solid colored traces identify major branches of processes that have extended toward the microhemorrhage. At subsequent time points, these cells (position over time indicated by circles with matching color) migrated along the path defined by the extended process. The path the cell migrated along is indicated with dashed lines of matching color. The yellow circles indicate nearby microglia that migrated into the region of interest, either from above or below this region or from the sides. Scale bar is 100 µm.

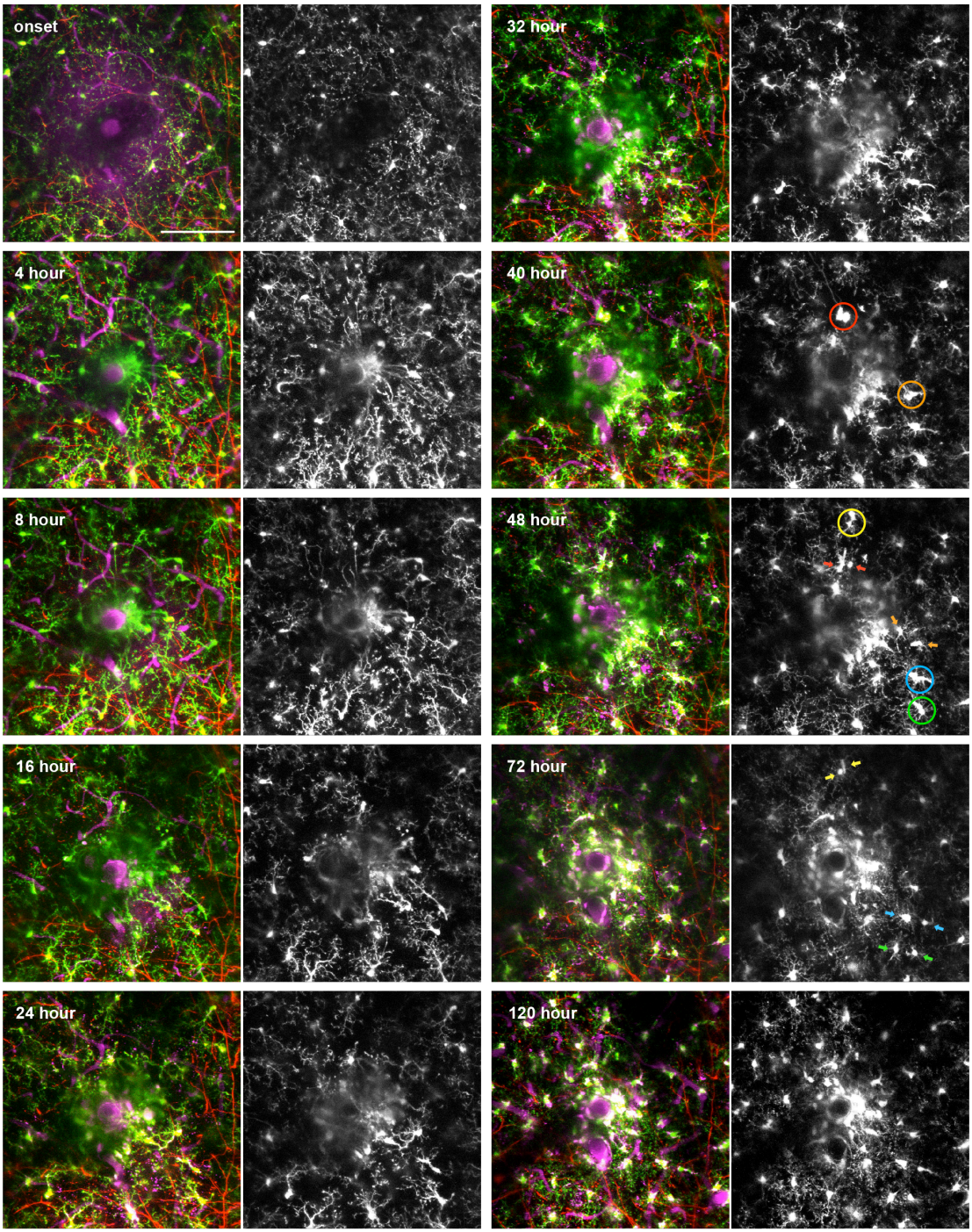
A
onset
32 hour
4 hour
40 hour
8 hour
48 hour
16 hour
72 hour
24 hour
120 hour

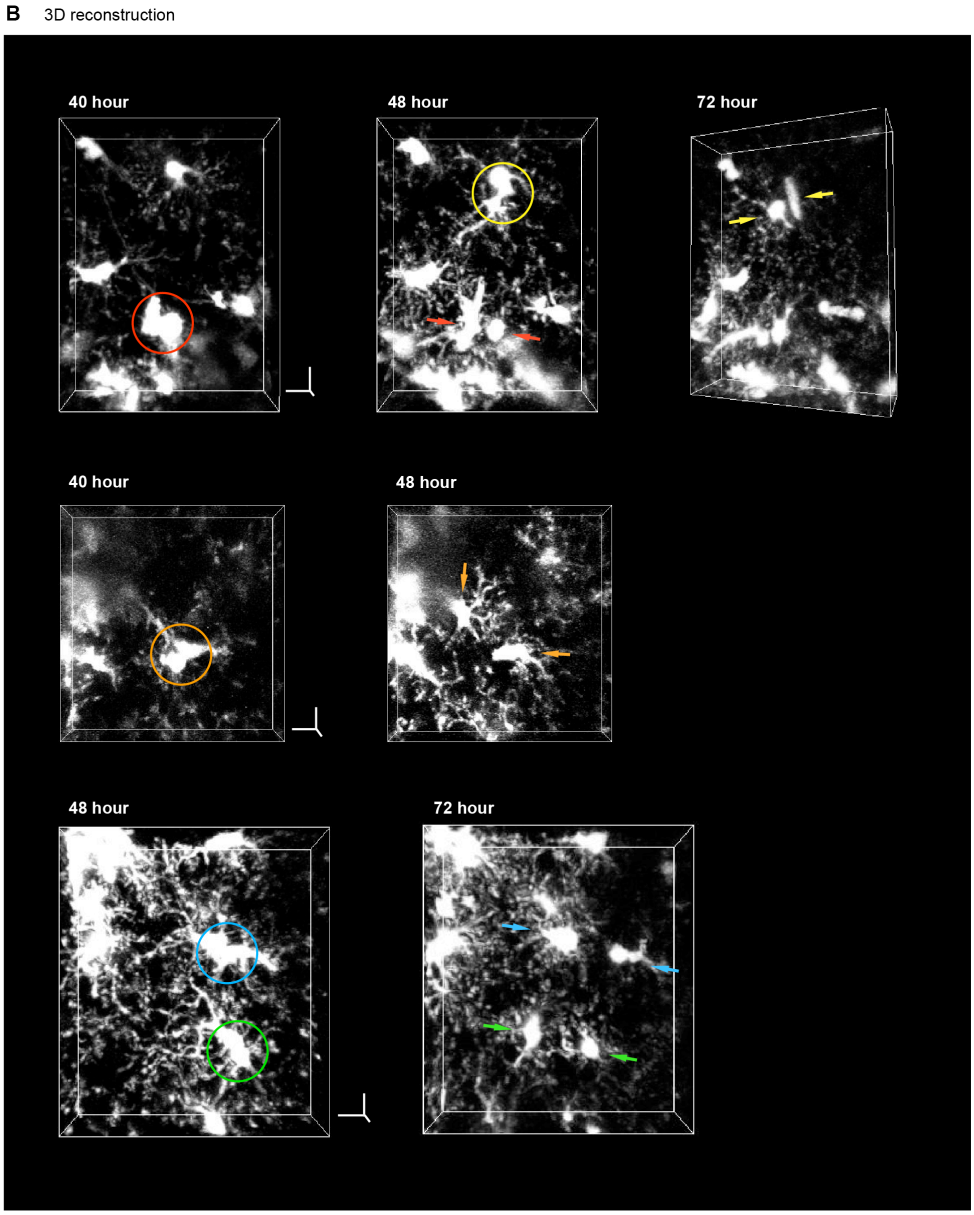

Supplementary figure 4.2 Daughter cells from a microglia proliferation event were observed only more than 40 hours after a microhemorrhage (**A**) Axial projections of 40-µm thick 2PEF image stacks over time after a microhemorrhage in a *Cx3cr1*$^{GFP/+}$ mouse (magenta, i.v. injected Texas Red dextran; green, GFP; red, YFP expressed under control of the Thy1 promoter to label Layer V pyramidal neurons and their axons and dendritic arbors, which were visible at this depth). Greyscale images show just GFP-labeled microglia. Colored circles indicate cells that will proliferate by the next time point. Arrows with matching colors indicate the pair of daughter cells. Scale bar is 100 µm. (**B**) Three-dimensional reconstructions of some of the microglia cell division events shown in (A). Colored circles and arrows indicate corresponding cells from (A). Scale bars are 10 µm.

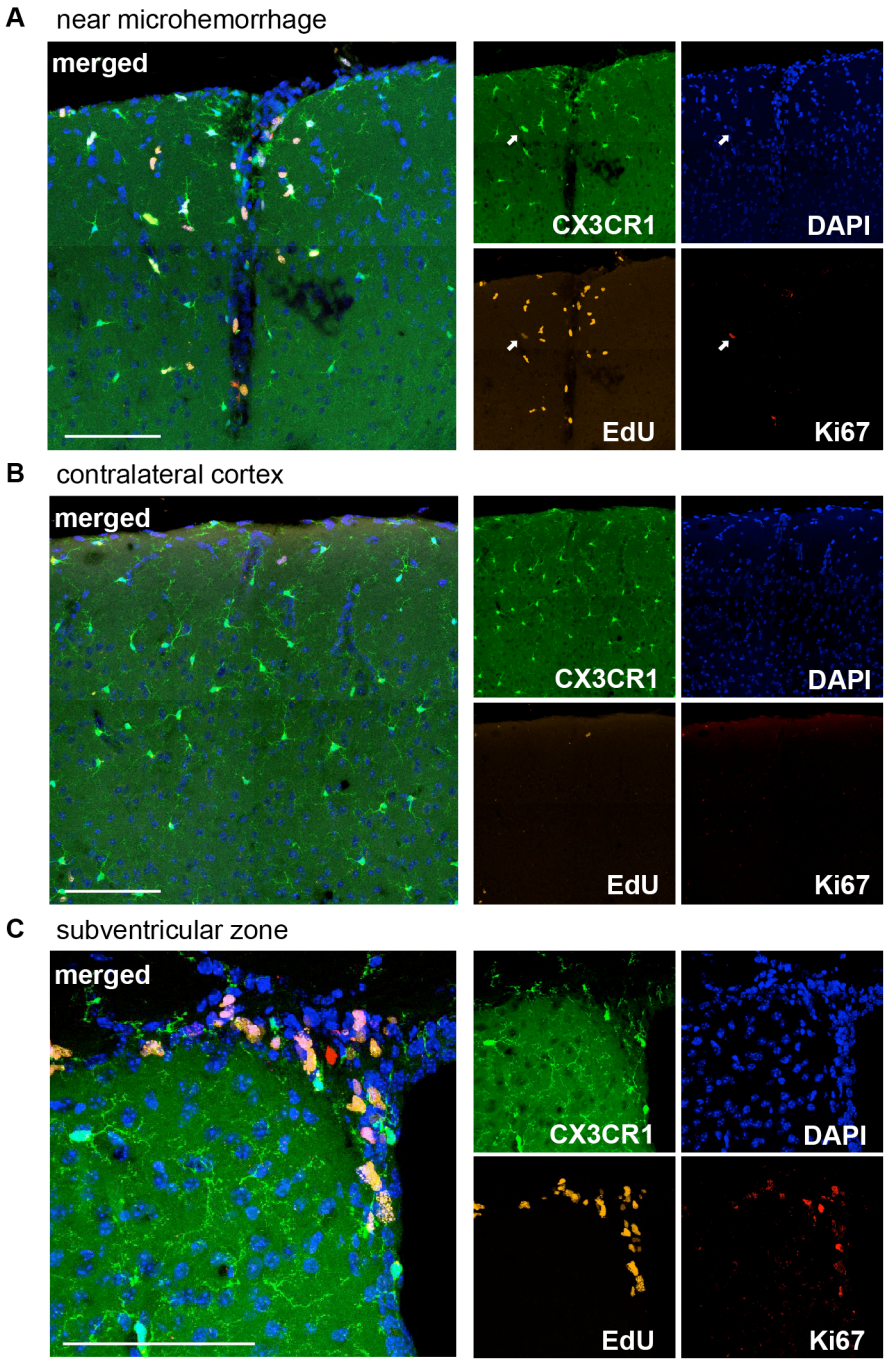

Supplementary figure 4.3 Microglia proliferation was observed in the region surrounding a microhemorrhage Histology images showing GFP-labeled microglia, DAPI labeled nuclei, EdU positive cells (EdU injected every eight hours for two days after microhemorrhage induction), and Ki67 expression (imunolabeled). (**A**) Section that intersects a microhemorrhage. The arrow indicates a cell that was labeled with EdU, Ki67, and GFP, indicating a microglia that was actively proliferating. (**B**) Negative control region from contralateral cortex. (**C**) Positive control region from sub-ventricular zone. Scale bars in a and b are 100 µm, in c it is 50 µm.

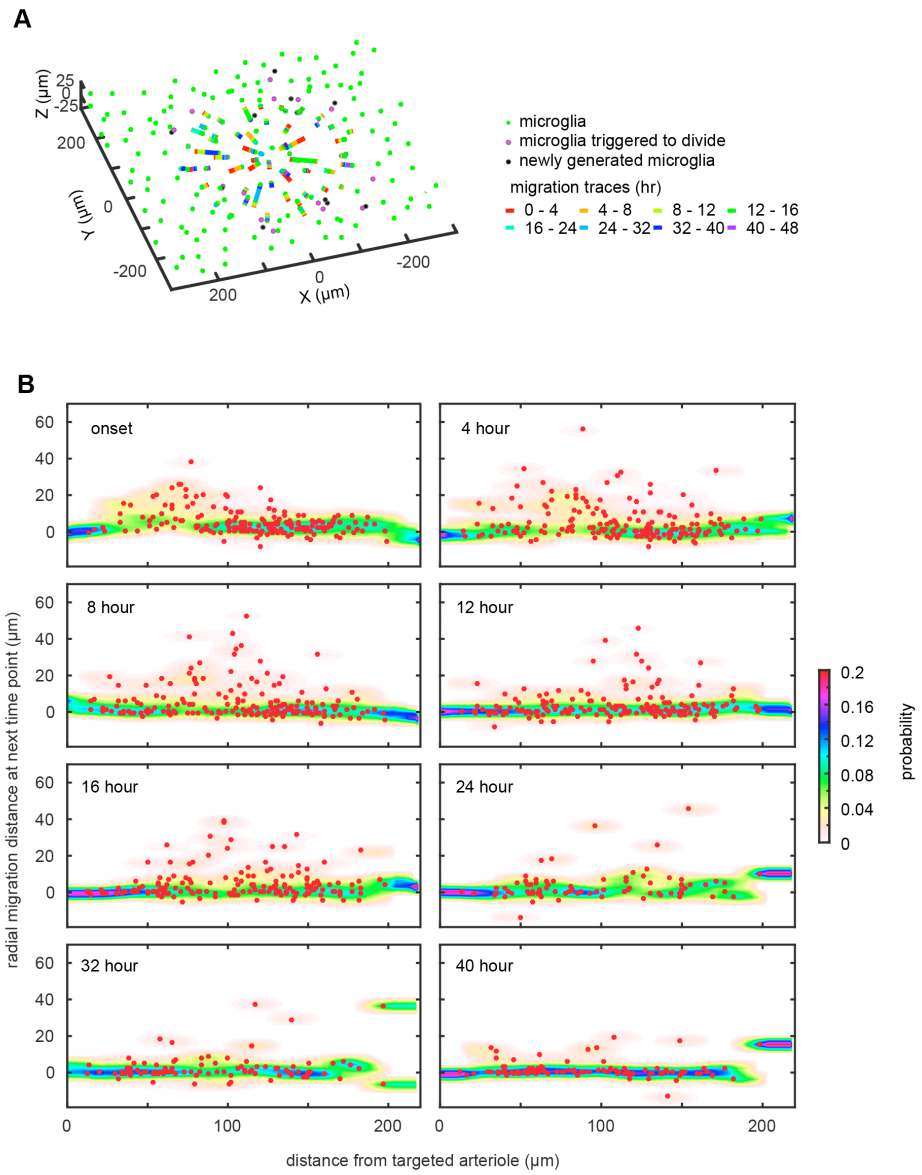

Supplementary figure 4.4 Microglia migration distance as a function of distance from the targeted arteriole and time after the injury (**A**) Example of one simulation showing coordinates of microglia at two days after the microhemorrhage and the migration traces of individual microglia. Microglia committed to division and those newly generated are also indicated. (**B**) Red dots indicate experimental measurements of microglia migration from in vivo imaging (e.g. Figure 4.3 C-E). The average migration distance from this same data is shown in Figure 4.3E. The color map shows the probability distribution of migration distance for a microglia at a given distance from, and time after, the microhemorrhage. This probability distribution was derived from the experimental data by calculating the density of points over a sliding window that was 5 µm high (migration distance) and 20 µm wide (distance from targeted arteriole) and then smoothing. This probability function was then used for the simulations shown in Figure 4.5.

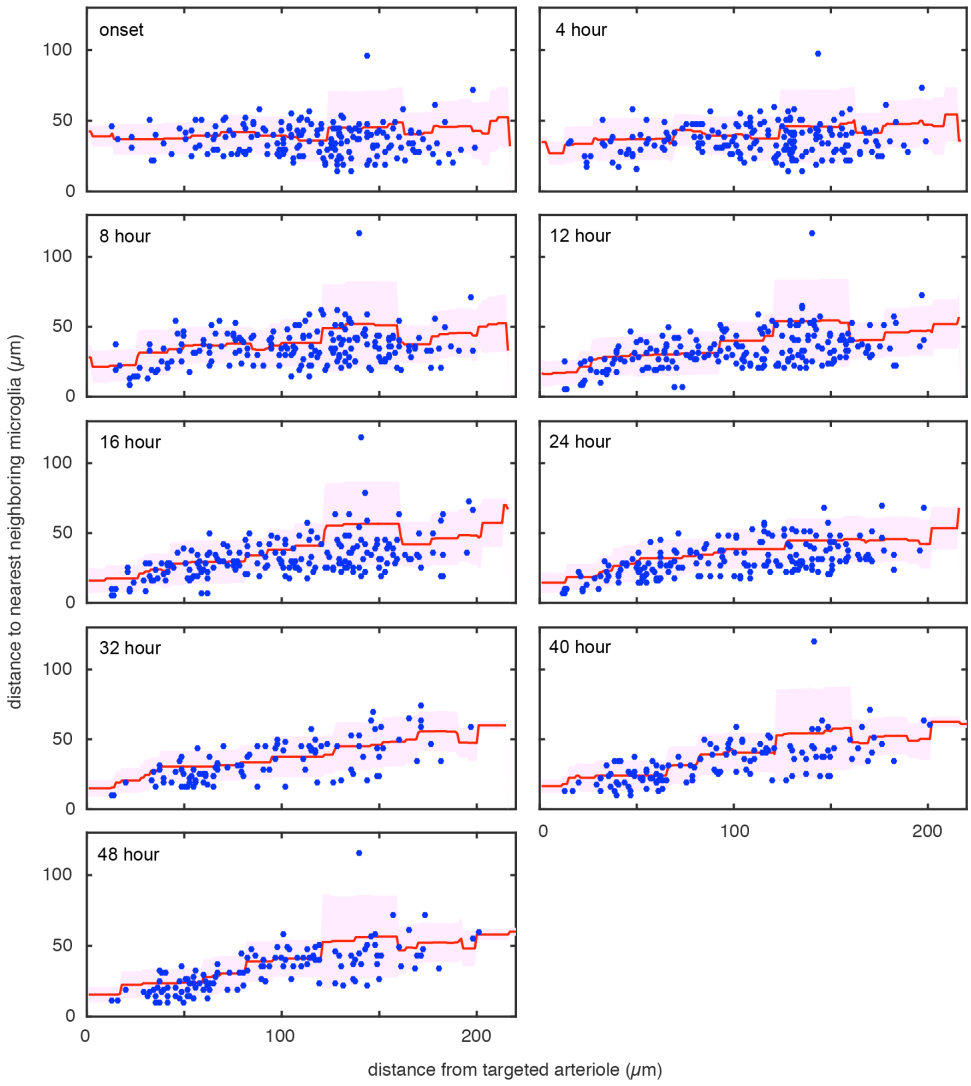

Supplementary figure 4.5 Distance to nearest neighboring microglia as a function of distance from the targeted arteriole and time after the injury Blue dots indicate experimental measurements of microglia nearest neighbor distances from the same data set used in Supplementary fig. 4.4 and Figure 4.3. Red line represents the mean, while the pink shadow represents ±1 SD from the mean.

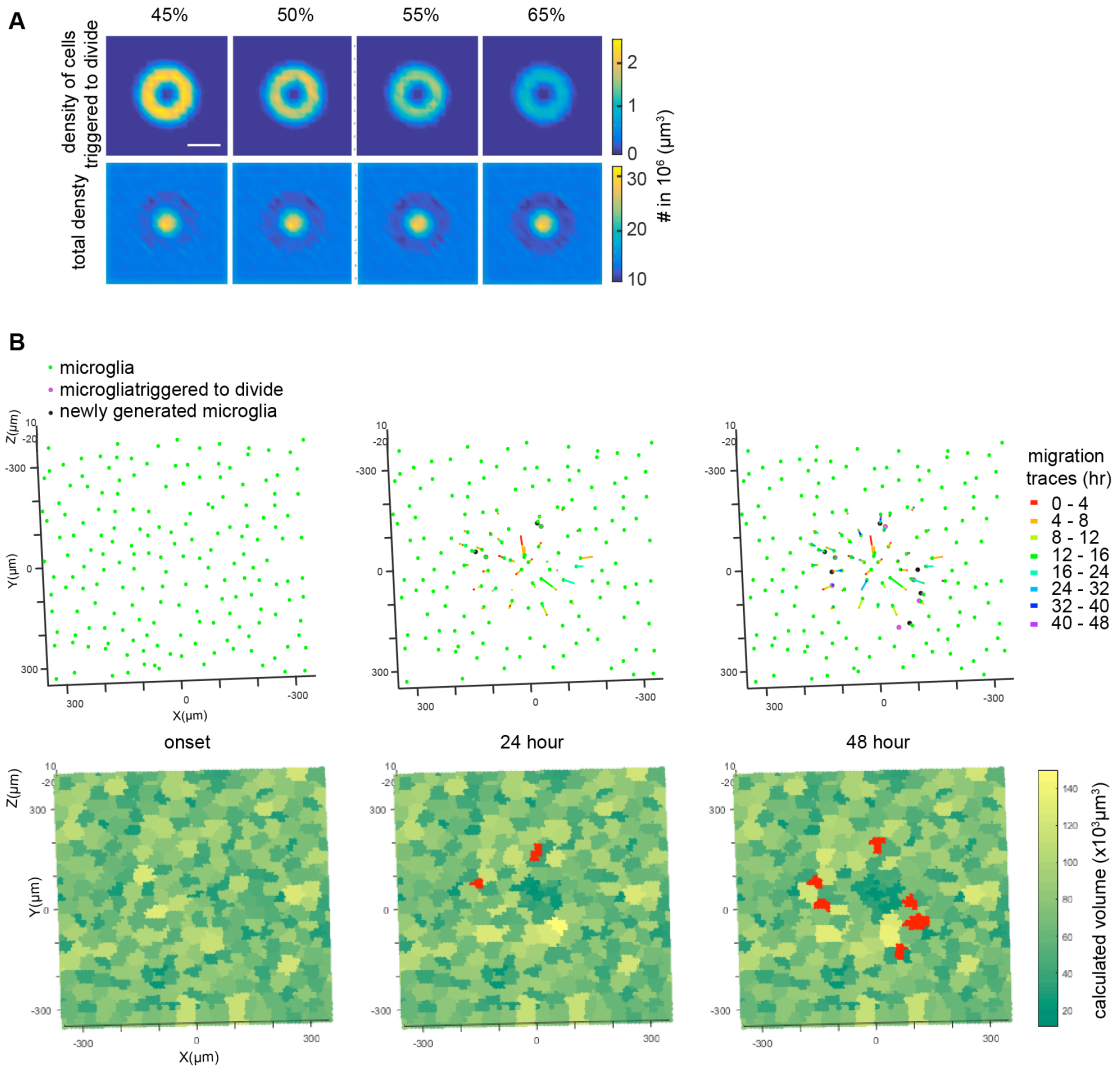

Supplementary figure 4.6 Calculation of the domain volume for each microglia using a topographic watershed algorithm over time after a microhemorrhage When microglia migrated toward the injury, the domain volume of some microglia increased. (**A**) Map of the total density of microglia (top) and of the density of microglia committed to division (bottom) at 48 hrs after a microhemorrhage using models where microglia proliferation occurs when the domain volume of a microglia increases by more than the percentage indicated at the top of each column. (**B**) In this simulation, when the volume increased by more than 50% for a microglia, it committed to dividing and created a new microglia 8 hr later. Bottom panels show the microglia territories (note the image shows just a cross-sectional plane of these volumes) and the color indicates the size of the domain volume. Top panels show microglia locations and migration traces. The pink (black) circles indicate microglia that have committed to divide (are newly born). The red facets in the left panels also indicate these new microglia. The hemorrhage is at the center of the frame.

4.5 Methods

4.5.1 Animals Experiments were performed in 20 to 40 week old transgenic mice on a C57BL/6J genetic background. Breeders were purchased from The Jackson Laboratory (CX3CR1-GFP #8451 [27], UBC-GFP #4353 [28], CCR2-RFP #17586 [29], Thy1-YFPH #3782 [30], wild-type) and animals were crossed and/or received bone marrow transplants to fluorescently label targeted cell types. All animal experiments were conducted in strict accordance with the recommendations in the Guide for the Care and Use of Laboratory Animals published by National Institutes of Health, and all animal procedures were approved by the Cornell University Institutional Animal Care and Use Committee (protocol numbers 2009-0043 and 2015-0029).

4.5.2 Bone marrow transplantation and chimerism Bone marrow chimeras were generated from transgenic and wild-type mice. Six to eight week old recipient mice were anesthesized with ketamine and xylazine (10 mg/100 g mouse weight ketamine; 1 mg/100 g xylazine; intraperitoneally). Mice were placed in a custom-built lead head shield and exposed to a lethal dose of gamma irradiation (10 Gy). Donor mice (2-4 months old) were deeply anesthetized using isoflurane (~3% in oxygen). Both femurs were removed and the animals euthanized by cervical dislocation. Bone marrow cells were flushed out from the femur with sterile saline and the density of cells was measured using a hemocytometer. Recipient mice received ~10^7 donor bone marrow cells through retro orbital injection 1-3 hr after irradiation. Nine weeks after the bone marrow transplant, ~100 μL of blood was collected from submandibular bleeding and the degree of chimerism was assessed by flow cytometry. We only used mice in which the

percentage of circulating white blood cells that came from the donated bone marrow was more than 63%. Although the head shielding we used here reduces the degree of chimerism achieved with the bone marrow transplant, it avoids gamma irradiation of the head, which could drive brain inflammation that may confound interpretation of the results [23, 31].

4.5.3 Chronic cranial window preparation Optical access to brain was achieved through a long-term implanted glass-covered cranial window, as described previously [32]. Animals were anesthetized using isoflurane (1.5–2% in oxygen) and placed on a feedback controlled heating blanket that maintained body temperature at 37˚C (50-7053P; Harvard Apparatus). Mice were given either glycopyrrolate (0.05 mg/100 g mouse weight; intramuscularly; Baxter, Inc.) or atropine sulfate (0.005 mg/100 g; subcutaneously; 54925-063-10, Med-Pharmex Inc.) to prevent lung secretions. Animals were also given dexamethasone (0.025 mg/100 g; subcutaneously; 07-808-8194, Phoenix Pharm Inc.) and ketoprofen (0.5 mg/100 g; subcutaneously; Zoetis Inc.) to reduce post-surgical inflammation and pain. A 6-mm diameter bilateral craniotomy was performed over parietal cortex using a dental drill. The exposed brain was covered with sterile saline and sealed with an 8-mm diameter glass coverslip using cyanoacrylate glue (Loctite 495; Henkel), tissue adhesive (70200742529, 3M^{TM}), and dental cement (Co-Oral-Ite Dental Mfg Co.). Animals were given a single injection of 5% weight/volume (w/v) glucose in saline at the conclusion of surgery (1 ml/100 g). All mice recovered at least 14 days from this surgery before in vivo imaging and microhemorrhage induction.

4.5.4 Multi channel *in vivo* two-photon excited fluorescence microscopy Mice were anesthetized with isofluorane (1.5–2% in oxygen) and placed in a stereotaxic apparatus equipped with a feedback-controlled heating pad. As above, mice were given either glycopyrrolate (0.05 mg/100 g; intramuscularly) or atropine sulfate (0.005 mg/100 g; subcutaneously) to prevent lung secretions. The blood plasma was labeled with either red or blue fluorescent dextran-conjugated dyes (2.5% w/v Texas-Red 70 kDa used with GFP positive cells, D-1830; 5% w/v Cascade-Blue 10 kDa used with RFP positive cells, D-1976; Invitrogen) diluted in sterile saline and retro-orbitally injected (50 µl) before imaging. Imaging was performed on a custom-built four-channel 2PEF microscope using the following emission filters (center wavelength/bandwidth): 417/60 (Cascade-Blue), 494/41 (GFP), 550/49 (YFP) and 641/75 nm (RFP and Texas-Red) separated with long-pass dichroics with cutoffs at 458, 520 and 562 nm. Excitation pulses came from a tunable Ti:Sapphire laser (Vision II, Coherent) set to a wavelength of 880 nm for imaging YFP, GFP, Texas-Red and to 800 nm for Cascade-Blue. An additional femtosecond laser at 1045 nm was used to image RFP (Yg fiber oscillator/amplifier; Satsuma; Amplitude Système). Image stacks were acquired through ScanImage software (version 3.8, Vidrio Technologies)[33]. Respiration was monitored throughout the imaging session and the isoflurane level was adjusted to maintain a steady breathing rate of ~1 Hz. During the imaging session, mice received an hourly dose of 5% w/v glucose in saline (1 ml/100 g). In animals that received atropine and not glycopyrrolate, the atropine was supplemented hourly (0.001 mg/100 g; subcutaneously).

4.5.5. Induction of microhemorrhage by femtosecond laser ablation Microhemorrhages were produced in the descending segment of penetrating arterioles (PAs) as previously described [4-6]. Femtosecond laser pulses were tightly focused (20x, 1.0 numerical aperture (NA), water immersion, cover glass corrected objective; W Plan-Apochromat (Zeiss)) on the outer edge of the vessel lumen of the targeted PA. We used 50-fs duration laser pulses produced by a Ti:sapphire regenerative amplifier (Legend 1 k USP; Coherent), pumped by a Q-switched laser (Evolution 15; Coherent) and seeded by a Ti:Sapphire oscillator (Chinhook; Kapteyn-Murnane Laboratories Inc.) that was pumped by a continuous wave laser (Verdi-V6; Coherent, Inc). Laser energy was controlled using neutral density filters. We began with a laser energy of ~50 nJ and targeted the PA about 100 μm beneath the cortical surface. A burst of 100 laser pulses (1 kHz repetition rate) was applied while we watched for extravasation of fluorescently-labeled blood plasma from the targeted vessel. If the vessel did not rupture then a burst of 200 and then 300 pulses with the same energy was applied. If the vessel still did not rupture, the laser pulse energy was increased by 50% and this process was repeated. This procedure ensured that the minimum laser energy required to rupture the targeted vessel was used to induce a microhemorrhage. Typical laser energies used to rupture PAs varied from 95 to 240 nJ, largely dependent on the depth at which the vessel was targeted. We acquired 2PEF image stacks with 1 μm axial spacing before and after inducing the hemorrhage, as well as movies of the hemorrhage induction process.

4.5.6 Analysis of microglia density after a microhemorrhage Microglia density was assessed using mice with microglia labeled with GFP and a reduced number of patrolling

monocytes labeled with GFP (*Cx3cr1*$^{GFP/+}$ with wild-type bone marrow). We imaged before and repeatedly over two weeks after the microhemorrhage. At each time point, multiple image stacks were taken at different distances from the microhemorrhage (center of imaging field at 0, 100, 300 μm away) and from a control region at least 1 mm away from any microhemorrhage. In each mouse, we made one or two microhemorrhages and imaged one control region. We manually identified the location of the cell body for each microglia in a 40-μm thick slab, centered at the depth of the microhemorrhage, across these imaging times and locations. As a means to assess the acute microglia response to the injury, we also categorized microglia as polarized if more than 50% of their processes were directed, within a 30-degree cone, toward the center of the microhemorrhage.

4.5.7 Counting infiltration of blood-derived inflammatory cells We used transgenic and bone-marrow transplanted mice to label specific circulating inflammatory cell populations, as described above. Because infiltrating inflammatory cells tended to stay close to the target vessel, we imaged just one location, centered on the lesion, over time. In addition to determining the location of each infiltrating cell, we further classed them as being perivascular if they surrounded or made contact with the target vessel and as being parenchymal if they did not.

4.5.8 Time lapse imaging for assessing microglia migration speed and proliferation To monitor the speed of microglia migration, we took 2PEF image stacks in *Cx3cr1*$^{GFP/+}$ or in *Cx3cr1*$^{GFP/+}$*Thy1-YFP* mice at the microhemorrhage site every four hours for 16 hours and then every eight hours up to 48 hours after the lesion. Animals were woken up

between each subsequent imaging session. The first imaging session took about two hours and involved baseline imaging, producing the microhemorrhage, and taking post-injury images. In subsequent imaging sessions, animals were anesthetized for ~20 min. while the same region was imaged. At these subsequent imaging sessions, animals were supplemented with additional dose of 5% w/v glucose in saline (1 mL/100 g) and of atropine (0.001 mg/100 g; subcutaneously), as well as with half the volume of fluorescent dextran dye (2.5% w/v Texas-Red; D-1830, Invitrogen) diluted in sterile saline and injected retro-orbitally (25 µl). We used the Rigid Registration plugin in FIJI to align all image stacks, using blood vessels and/or dendritic arbors (in animals with *Thy1-YFP*) as alignment guides. Because not all microglia migrated and because those that did tended to not migrate very far (<25 µm) between time points, it was possible to identify each individual microglia across each imaging time point to determine their migration paths. We also observed microglia proliferation, characterized by an elongated cell body shape and then two daughter cells at that location in the next imaging session (and with all neighboring microglia accounted for).

4.5.9 Assessment of microglia proliferation using post-mortem histology To assess microglia proliferation, we placed microhemorrhages in mice as described above and then gave intraperitoneal injections of 5-ethynyl-2'-deoxyuridine (EdU; 2 mg/100 g) every 8 hr for two days. After the 6^{th} injection, mice were sacrificed for histological analysis. Animals were transcardially perfused with 15 ml of phosphate buffered saline (PBS) (Sigma-Aldrich) followed by 30 ml of 4% w/v paraformaldehyde (PFA) (Fischer Scientific) in PBS. Brains were extracted, stored overnight in in 4% PFA in PBS at 4°C,

then in 15% w/v sucrose in PBS for 8 hr at 4°C, followed by 24 hr in 30% sucrose, and then in 60% sucrose until sectioning. We used a fiducial marking procedure to unambiguously identify individual microhemorrhages in the tissue sections. Briefly, fiducial marks were made just lateral to the edges of the craniotomy by insertion of a 30-gauge needle. Brains were then briefly immersed in a dilute solution of Toluidine Blue, which labeled mast cells on the brain surface and enabled us to visualize the large surface blood vessels as well as the fiducial marks. The microhemorrhage locations were known relative to the large surface vessels from 2PEF images and the Toluidine Blue stained image allowed us to define the location of the fiducials relative to the large surface vessels, and therefore the location of the microhemorrhages relative to the fiducials. The tissue was then frozen and cut into 20-μm thick coronal sections on a cryostat and mounted onto microscope slides. The fiducial marks were found in the series of brain sections and used to identify the tissue sections that went through a microhemorrhage. We used a kit to detect EdU-labeled cells (Click-iT EdU, C10340, Invitrogen) in the tissue sections. In addition, we immunolabeled for expression of Ki67, a protein expressed during active cell proliferation, using a rabbit anti-Ki67 monoclonal primary antibody at 1:100 dilution (GTX16667, GeneTex) with a goat anti-rabbit Alexa flour 594 conjugated secondary antibody at 1:200 dilution (A-11037, Invitrogen). Stained slides were mounted using an anti-fade mounting medium that contained DAPI (Vetashield, H-1200, Vector Laboratories). Fluorescent images were collected on an inverted confocal fluorescence microscope (LSM880, Zeiss) using a 40x/1.1 NA long working distance water immersion objective (421767-9971-711, Zeiss).

4.5.10 Assessing astrocyte activation using post-mortem histology For astrocyte labeling, we scarified *Cx3cr1*$^{GFP/+}$ mice at 2, 7, 14, and 21 days after the induction of a microhemorrhage and slides with microhemorrhages (identified as above) were stained for GFAP using a chicken anti-GFAP polyclonal antibody at 1:1000 dilution (ab4674, abcam) with a goat anti-chicken Alexa flour 594 conjugated secondary antibody at 1:200 dilution (A-11042, Invitrogen). Fluorescence images of microglia (GFP) and astrocytes (Alexa flour 594) were collected on the same inverted confocal microscope.

4.5.11 Modeling microglia density change after microhemorrhage We developed a simple model of the microglia response to a brain microhemorrhage using our data on microglia migration and proliferation. *In vivo* measurements from 11 *Cx3cr1*$^{GFP/+}$ mice revealed a microglia density of $1.3\pm0.3\times10^4$ cells/mm^3, and a minimum nearest neighbor distance between microglia of 37±11 μm. In our simulation, we first seeded microglia at random locations in an 800 × 800 × 50 μm volume, while matching this cell density and spacing. We used *in vivo* measurements of microglia migration after the microhemorrhage (Figure 4.3C-E) to calculate a probability distribution of the radial migration distance for microglia at different distances from and times after the microhemorrhage (Supplementary fig. 4.4B; smoothed over 20 μm in distance from the lesions and 5 μm in migration distance). This probability distribution was used to determine the radial migration of each microglia every 4 hr for 16 hrs and then every 8 hr until 48 hr after the lesion. From our *in vivo* imaging, we also quantified the minimum nearest-neighbor microglia spacing as a function of distance from and time after the lesion (Supplementary fig. 4.5; smoothed over 20 μm in distance from the lesions and 5

μm in migration distance). If the migration of a microglia placed it closer to another microglia than one standard deviation below the mean of this nearest-neighbor microglia spacing then we determined a new migration distance for that cell.

The proliferation probability and the time for microglia cell division was determined from the number of EdU and Ki67 positive microglia in the histology images. Only cells that were actively in the cell cycle when the animal was sacrificed would express Ki67. With the EdU dosing strategy we used, all cells that had entered the cell cycle over the full 48 hours after the injury, as well as all daughter cells, would be labeled. The number of Ki67, $N_{Ki67,}$ and EdU positive cells, $N_{EdU,}$ at a time, $T,$ after the microhemorrhage are thus given by:

$$N_{Ki67}(r) = \sum_{t=T-\tau}^{T} R(r) * N * (1 - R(r))^t$$

$$N_{EdU}(r) = \sum_{t=1}^{T-\tau} 2 * R(r) * N * (1 - R(r))^t + \sum_{t=T-\tau}^{T} R(r) * N * (1 - R(r))^t$$

where N is the number of microglia at baseline, τ is the time required for microglia cell division, $R(r)$ is the probability of a microglia being triggered to proliferate and is dependent on r, the distance from the microhemorrhage, and t is time after the lesion given in discrete steps (hrs). This model assumes that within this time frame (maximum simulation times of T=48 hrs), the daughter cells of a microglia proliferation event do not divide again. We then calculated $R(r)$ and τ to match the spatially dependent fraction of

microglia that were EdU positive (Figure 4.4D) and the ratio of Ki67 to EdU positive microglia ($N_{Ki67}/N_{EdU} = 0.084$). At each time point in the simulation, we used the distance-dependent probability of a microglia entering the cell cycle, $R(r)$, to identify cells that will later divide. We then seeded a new microglia at a location ~30 μm away after a time, τ. We averaged the results of 1,000 simulations.

4.5.12 Modeling a causal relationship between microglia density change and proliferation To examine the hypothesis that microglial proliferation was initiated by a density changes, we then used an alternate model for microglia proliferation that depended only on local changes in microglia density. After seeding microglia, we assigned each image voxel to the closest microglia, thereby defining a domain volume for each microglia. We then ran the simulation with microglia migration handled as described above. At each time step, we recalculated the domain volume for each microglia. If the domain volume increased by more than a specified fraction then that cell was flagged to divide and after a time, τ, a new microglia was seeded ~30 μm away.

4.5.13 Image, data, and statistical analysis All 2PEF images were analyzed using FIJI [34]. For the generation of images of fluorescent species with overlapping spectral profiles, we used a custom linear unmixing code written in Matlab. Image manipulations were limited to linear adjustments of image contrast. All displayed images represent maximal projections of 2PEF image stacks except for the single plane movie frames in Figure 4.1A and the renderings in Figure 4.1A and Supplementary fig. 4.2B, which used

Volocity (PerkinElmer Inc) and Imaris (Bitplane), respectively. Data in all plots represents the mean and error bars represent the standard deviation.

4.6 Acknowledgments

This work was supported by the National Institutes of Health grant NS080098 (C.S.) and the American Heart Association grant 16PRE27600010 (S.A.). Confocal images were acquired through the Cornell University Biotechnology Resource Center, with NYSTEM (CO29155) and NIH (S10OD018516) funding for the shared Zeiss LSM880 confocal/multiphoton microscope. We thank Sylvie Allen and Kevin Yager in the Cornell Center for Animal Resources and Education for assistance with the mouse irradiation for bone marrow transplants.

4.7 Author Contributions

S.A. designed and performed all the experiments and simulations. J.A., N.N., and C.S. conceived, designed, and supervised the study. S.A. and C.S. wrote the paper with contributions and comments from all authors.

4.8 Competing Financial Interests

The authors declare no competing financial interests.

REFERENCES

[1] Z. Ungvari, S. Tarantini, A. C. Kirkpatrick, A. Csiszar, and C. I. Prodan, "Cerebral microhemorrhages: mechanisms, consequences, and prevention," *Am J Physiol Heart Circ Physiol,* vol. 312, pp. H1128-h1143, Jun 01 2017.

[2] A. F. Wiegman, I. B. Meier, N. Schupf, J. J. Manly, V. A. Guzman, A. Narkhede*, et al.*, "Cerebral microbleeds in a multiethnic elderly community: demographic and clinical correlates," *J Neurol Sci,* vol. 345, pp. 125-30, Oct 15 2014.

[3] M. M. F. Poels, M. A. Ikram, A. van der Lugt, A. Hofman, W. J. Niessen, G. P. Krestin*, et al.*, "Cerebral microbleeds are associated with worse cognitive function The Rotterdam Scan Study," *Neurology,* vol. 78, pp. 326-333, Jan 2012.

[4] N. Nishimura, C. B. Schaffer, B. Friedman, P. S. Tsai, P. D. Lyden, and D. Kleinfeld, "Targeted insult to subsurface cortical blood vessels using ultrashort laser pulses: three models of stroke," *Nature Methods,* vol. 3, pp. 99-108, Feb 2006.

[5] N. L. Rosidi, J. Zhou, S. Pattanaik, P. Wang, W. Jin, M. Brophy*, et al.*, "Cortical microhemorrhages cause local inflammation but do not trigger widespread dendrite degeneration," *PLoS One,* vol. 6, p. e26612, 2011.

[6] F. A. Cianchetti, D. H. Kim, S. Dimiduk, N. Nishimura, and C. B. Schaffer, "Stimulus-Evoked Calcium Transients in Somatosensory Cortex Are Temporarily Inhibited by a Nearby Microhemorrhage," *Plos One,* vol. 8, May 28 2013.

[7] M. Fisher, S. French, P. Ji, and R. C. Kim, "Cerebral microbleeds in the elderly: a pathological analysis," *Stroke,* vol. 41, pp. 2782-5, Dec 2010.

[8] L. Garcia-Bonilla, G. Faraco, J. Moore, M. Murphy, G. Racchumi, J. Srinivasan*, et al.*, "Spatio-temporal profile, phenotypic diversity, and fate of recruited monocytes into the post-ischemic brain," *J Neuroinflammation,* vol. 13, p. 285, Nov 04 2016.

[9] A. Nimmerjahn, F. Kirchhoff, and F. Helmchen, "Resting microglial cells are highly dynamic surveillants of brain parenchyma in vivo," *Science,* vol. 308, pp. 1314-8, May 27 2005.

[10] S. A. Liddelow and B. A. Barres, "Reactive Astrocytes: Production, Function, and Therapeutic Potential," *Immunity,* vol. 46, pp. 957-967.

[11] A. Shemer, D. Erny, S. Jung, and M. Prinz, "Microglia Plasticity During Health and Disease: An Immunological Perspective," *Trends Immunol,* vol. 36, pp. 614-24, Oct 2015.

[12] C. E. Loscher, K. H. Mills, and M. A. Lynch, "Interleukin-1 receptor antagonist exerts agonist activity in the hippocampus independent of the interleukin-1 type I receptor," *J Neuroimmunol,* vol. 137, pp. 117-24, Apr 2003.

[13] E. C. Beattie, D. Stellwagen, W. Morishita, J. C. Bresnahan, B. K. Ha, M. Von Zastrow*, et al.*, "Control of synaptic strength by glial TNFalpha," *Science,* vol. 295, pp. 2282-5, Mar 22 2002.

[14] J. T. Rogers, J. M. Morganti, A. D. Bachstetter, C. E. Hudson, M. M. Peters, B. A. Grimmig*, et al.*, "CX3CR1 deficiency leads to impairment of hippocampal cognitive function and synaptic plasticity," *J Neurosci,* vol. 31, pp. 16241-50, Nov 9 2011.

[15] A. M. Kaindl, V. Degos, S. Peineau, E. Gouadon, V. Chhor, G. Loron*, et al.*, "Activation of microglial N-methyl-D-aspartate receptors triggers inflammation and neuronal cell death in the developing and mature brain," *Ann Neurol,* vol. 72, pp. 536-49, Oct 2012.

[16] H. Wake, A. J. Moorhouse, S. Jinno, S. Kohsaka, and J. Nabekura, "Resting Microglia Directly Monitor the Functional State of Synapses In Vivo and Determine the Fate of Ischemic Terminals," *Journal of Neuroscience,* vol. 29, pp. 3974-3980, Apr 1 2009.

[17] G. Szalay, B. Martinecz, N. Lenart, Z. Kornyei, B. Orsolits, L. Judak*, et al.*, "Microglia protect against brain injury and their selective elimination dysregulates neuronal network activity after stroke," *Nat Commun,* vol. 7, p. 11499, May 03 2016.

[18] S. A. Liddelow, K. A. Guttenplan, L. E. Clarke, F. C. Bennett, C. J. Bohlen, L. Schirmer*, et al.*, "Neurotoxic reactive astrocytes are induced by activated microglia," *Nature,* vol. 541, pp. 481-487, Jan 26 2017.

[19] D. Davalos, J. Grutzendler, G. Yang, J. V. Kim, Y. Zuo, S. Jung*, et al.*, "ATP mediates rapid microglial response to local brain injury in vivo," *Nat Neurosci,* vol. 8, pp. 752-8, Jun 2005.

[20] M. Fuhrmann, T. Bittner, C. K. Jung, S. Burgold, R. M. Page, G. Mitteregger*, et al.*, "Microglial Cx3cr1 knockout prevents neuron loss in a mouse model of Alzheimer's disease," *Nat Neurosci,* vol. 13, pp. 411-3, Apr 2010.

[21] S. Hong, V. F. Beja-Glasser, B. M. Nfonoyim, A. Frouin, S. Li, S. Ramakrishnan, *et al.*, "Complement and microglia mediate early synapse loss in Alzheimer mouse models," *Science,* vol. 352, pp. 712-6, May 06 2016.

[22] G. Raivich, M. Bohatschek, C. U. Kloss, A. Werner, L. L. Jones, and G. W. Kreutzberg, "Neuroglial activation repertoire in the injured brain: graded response, molecular mechanisms and cues to physiological function," *Brain Res Brain Res Rev,* vol. 30, pp. 77-105, Jul 1999.

[23] A. Mildner, H. Schmidt, M. Nitsche, D. Merkler, U. K. Hanisch, M. Mack, *et al.*, "Microglia in the adult brain arise from Ly-6ChiCCR2+ monocytes only under defined host conditions," *Nat Neurosci,* vol. 10, pp. 1544-53, Dec 2007.

[24] B. Ajami, J. L. Bennett, C. Krieger, W. Tetzlaff, and F. M. Rossi, "Local self-renewal can sustain CNS microglia maintenance and function throughout adult life," *Nat Neurosci,* vol. 10, pp. 1538-43, Dec 2007.

[25] K. Askew, K. Li, A. Olmos-Alonso, F. Garcia-Moreno, Y. Liang, P. Richardson, *et al.*, "Coupled Proliferation and Apoptosis Maintain the Rapid Turnover of Microglia in the Adult Brain," *Cell Rep,* vol. 18, pp. 391-405, Jan 10 2017.

[26] T. L. Tay, D. Mai, J. Dautzenberg, F. Fernandez-Klett, G. Lin, Sagar, *et al.*, "A new fate mapping system reveals context-dependent random or clonal expansion of microglia," vol. 20, pp. 793-803, Jun 2017.

[27] S. Jung, J. Aliberti, P. Graemmel, M. J. Sunshine, G. W. Kreutzberg, A. Sher, *et al.*, "Analysis of fractalkine receptor CX(3)CR1 function by targeted deletion and green fluorescent protein reporter gene insertion," *Mol Cell Biol,* vol. 20, pp. 4106-14, Jun 2000.

[28] B. C. Schaefer, M. L. Schaefer, J. W. Kappler, P. Marrack, and R. M. Kedl, "Observation of antigen-dependent CD8+ T-cell/ dendritic cell interactions in vivo," *Cell Immunol,* vol. 214, pp. 110-22, Dec 15 2001.

[29] N. Saederup, A. E. Cardona, K. Croft, M. Mizutani, A. C. Cotleur, C. L. Tsou*, et al.*, "Selective chemokine receptor usage by central nervous system myeloid cells in CCR2-red fluorescent protein knock-in mice," *PLoS One,* vol. 5, p. e13693, Oct 27 2010.

[30] G. Feng, R. H. Mellor, M. Bernstein, C. Keller-Peck, Q. T. Nguyen, M. Wallace*, et al.*, "Imaging neuronal subsets in transgenic mice expressing multiple spectral variants of GFP," *Neuron,* vol. 28, pp. 41-51, Oct 2000.

[31] T. Furuya, R. Tanaka, T. Urabe, J. Hayakawa, M. Migita, T. Shimada*, et al.*, "Establishment of modified chimeric mice using GFP bone marrow as a model for neurological disorders," *Neuroreport,* vol. 14, pp. 629-31, Mar 24 2003.

[32] A. Holtmaat, T. Bonhoeffer, D. K. Chow, J. Chuckowree, V. De Paola, S. B. Hofer*, et al.*, "Long-term, high-resolution imaging in the mouse neocortex through a chronic cranial window," *Nat Protoc,* vol. 4, pp. 1128-44, 2009.

[33] T. A. Pologruto, B. L. Sabatini, and K. Svoboda, "ScanImage: Flexible software for operating laser scanning microscopes," *BioMedical Engineering OnLine,* vol. 2, p. 13, 2003.

[34] J. Schindelin, I. Arganda-Carreras, E. Frise, V. Kaynig, M. Longair, T. Pietzsch*, et al.*, "Fiji: an open-source platform for biological-image analysis," *Nat Methods,* vol. 9, pp. 676-82, Jun 28 2012.

CHAPTER FIVE

LABEL FREE MEASUREMENT OF CORTICAL BLOOD FLOW SPEED IN INDIVIDUAL VESSELS USING THIRD HARMONIC GENERATION MICROSCOPY

5.1 Introduction

In recent decades, multi-photon excitation fluorescence (MPEF) microscopy has become one of the most important imaging tools used in biomedical research by enabling deeper imaging in scattering tissue with high resolution and contrast [1-3]. With the development of various fluorescent agents combined with advancements in genetic engineering, a detectable fluorescent signal can be used to monitor cell structure and function in a living animal [4-7]. As a result, the advent of nonlinear microscopy opened an era of minimally invasive in vivo imaging to study cellular structures, processes and responses to systematic manipulations in their natural state. Furthermore, three photon-excited fluorescence (3PEF) has increased imaging depth up to 900μm from the cortical surface, enabling deep brain imaging [8, 9]. However, both genetic modulation of animals for expressing fluorescent proteins and injection of various fluorescent dyes can systemically and functionally modify the exact nature of biological phenomena to a degree that is not fully understood.

Harmonic generation is a coherent (phase-preserving) process characteristic of a resonant material and requires no actual absorption of laser photons. Therefore, the laser-induced harmonic generation (HG) leaves no energy deposition in the impacted material. A number of endogenous biological structures possess a structural property that emits second harmonic generation (SHG) [10, 11] and third harmonic generation (THG) [12-15] when its phase matches the phase of the excitation source. Using these endogenous structures therefore avoids common issues associated with fluorescence excitation microscopy, such as photodamage, phototoxicity, photobleaching, and toxicity from fluorescent dyes.

The traditional method for measuring blood cell speed in vivo is achieved by labeling blood plasma with an intravenous injection of fluorescence-conjugated dextran dyes and laser scanning a line along a vessel to create a distance-time image [16-18]. Here, the negative signal indicates the presence of a blood cell, which form angled stripes due to the temporal displacement of blood cells. The slope of the stripes can then be used to calculate blood cell speed. Red blood cells (RBCs) and leukocytes have been shown to express high THG signals [19, 20]. Our preliminary observations suggest that the THG signal from 1300nm excitation produces greater blood cell contrast compared to 3PEF of dextran-conjugated dyes when measuring blood flow speed. Therefore, we demonstrate the use of THG microscopy as a label-free live brain-imaging tool to measure cortical blood flow speed, and examined the changes to cortical blood flow from exogenous contrast agent, fluorescein isothiocyanate (FITC) conjugated dextran dye.

5.2 Materials and Methods

5.2.1 Animals Experiments were performed in 4 month-old, wild-type mice (C57BL/6J). All animal experiments were conducted in strict accordance with the recommendations in the Guide for the Care and Use of Laboratory Animals published by National Institutes of Health, and all animal procedures were approved by the Cornell University Institutional Animal Care and Use Committee (protocol numbers 2009-0043 and 2015-0029).

5.2.2 Chronic cranial window preparation Optical access to the brain was achieved via a cranial window using an implanted 8mm glass coverslip, as described previously [21]. Animals were anesthetized using isoflurane (1.5–2% in oxygen) and placed on a

feedback-controlled heating pad that maintained body temperature at 37˚C (50-7053P; Harvard Apparatus). Mice were given atropine sulfate (0.005 mg/100 g; subcutaneously; 54925-063-10, Med-Pharmex Inc.) to reduce buildup of lung secretions. Animals were also given dexamethasone (0.025 mg/100 g; subcutaneously; 07-808-8194, Phoenix Pharm Inc.) and ketoprofen (0.5 mg/100 g; subcutaneously; Zoetis Inc.) to reduce post-surgical inflammation and pain, respectively. A 6-mm diameter bilateral craniotomy was performed over parietal cortex using a dental drill. The exposed brain was covered with sterile saline and sealed with an 8-mm diameter glass coverslip using cyanoacrylate glue (Loctite 495; Henkel), tissue adhesive (70200742529, 3M^{TM}) and dental cement (Co-Oral-Ite Dental Mfg Co.). Animals were given a single subcutaneous injection of 5% weight/volume (w/v) glucose in saline at the conclusion of surgery (1 ml/100 g). Following surgery, mice were given at least 21 days to recover before in vivo imaging.

5.2.3 Multi channel *in vivo* multi-photon excited microscopy Mice were anesthetized with isofluorane (1.5–2% in oxygen) and placed in a stereotaxic apparatus equipped with a feedback-controlled heating pad. As above, mice were given atropine sulfate (0.005 mg/100 g; subcutaneously) to reduce buildup of lung secretions. Imaging was performed on a custom-built three-channel multiphoton microscope using the following emission filters (center wavelength/bandwidth): 417/60nm, 494/41nm, 550/49nm separated by long-pass dichroics with cutoffs at 458nm and 520nm. To generate 1300nm laser light to induce 3PEF and THG, an optical parametric amplifier (OPA) (Coherent, Opera-F) was seeded by a diode-pumped femtosecond laser (60 μJ/pulse at 1 MHz; Coherent, Monaco). A tunable Ti:Sapphire laser (Vision II, Coherent), set to a wavelength of 800nm, was

used for 2PEF. Image stacks were acquired through ScanImage software (version 3.8, Vidrio Technologies) [22]. Respiratory rate was monitored throughout the imaging session and the isoflurane level was adjusted to maintain a steady respiratory rate of ~1 Hz. During the imaging session, mice received an hourly dose of 5% w/v glucose in saline (1 ml/100 g; subcutaneously) and atropine (0.001 mg/100 g; subcutaneously).

5.2.4 Repeated imaging with and without dextran-conjugated fluorescent dye For the first imaging session, blood plasma was labeled with a high concentration of green fluorescent dextran-conjugated dye (5% w/v FITC 2 MDa, 52471 Sigma) diluted in sterile saline and retro-orbitally injected (100 µl) prior to imaging. A shallow wide-field map of the cortical vasculature visible through the cranial window was taken using a 4x objective (XLFluor 0.28NA Zeiss). All line scan data, z-stacks above and below measured vessels, and z-stacks from the surface of the brain into the deep cortex was taken through a higher magnification 25x objective (Olympus XLPlan N 1.05 NA) with the 1300nm source and carefully mapped onto the projection of the lower 4x magnification map. To identify different vessel classes, we looked at the angle of the centerline RBC flow from line-scan measurements with regard to the vessel's geometric structure and branching direction either into or out from the brain [23]. Arterioles and venules were determined first, and ascending and descending branches were morphologically traced for blood flow measurements. All line scans were performed for at least 35 seconds for each individual vessel. Mice recovered for at least one day to allow washout of the dextran dye from the circulatory system. The subsequent imaging

session used only THG signals for measuring blood flow of all previously examined vessels, using the 4x surface map as a guide to relocate them.

5.2.5 Image analysis All image stacks were processed and analyzed using FIJI. Line scans were analyzed using a custom written code in MATLAB.

5.3 Results

To investigate the feasibility of *in vivo* 3PEF and THG microscopy, we first explored the limit of imaging depth. Through a chronic cranial window placed at least 3 weeks prior to imaging, we could achieve a depth of ~1mm. In about half of the mice imaged, we could go deep into the white matter, ~900μm below the surface (Figure 5.1A). The other half had clear imaging up to 830μm in depth. THG produced high contrast of individual blood cells in all measured vessels. Deeper into the cortex, line scan analysis was performed on capillaries 8μm in diameter or less (Figure 5.1). There was a mild trend of increasing blood flow speed and a decrease in the contrast between signal and noise due to scattering as a function of depth (Figure 5.1B and C).

Matching vessels could be identified from previous imaging sessions using the THG signal and 4x surface map. In general, the THG signal contrasted well against the background throughout the vasculature. Bigger vessels on the surface (diameter >20μm) had slightly less THG signal likely due to the absorption of THG by RBCs (Figure 5.2). However, these vessels were still identifiable based on the THG signal lining the vessel wall. In capillary beds, blood vessel walls do not produce THG signal, and therefore are

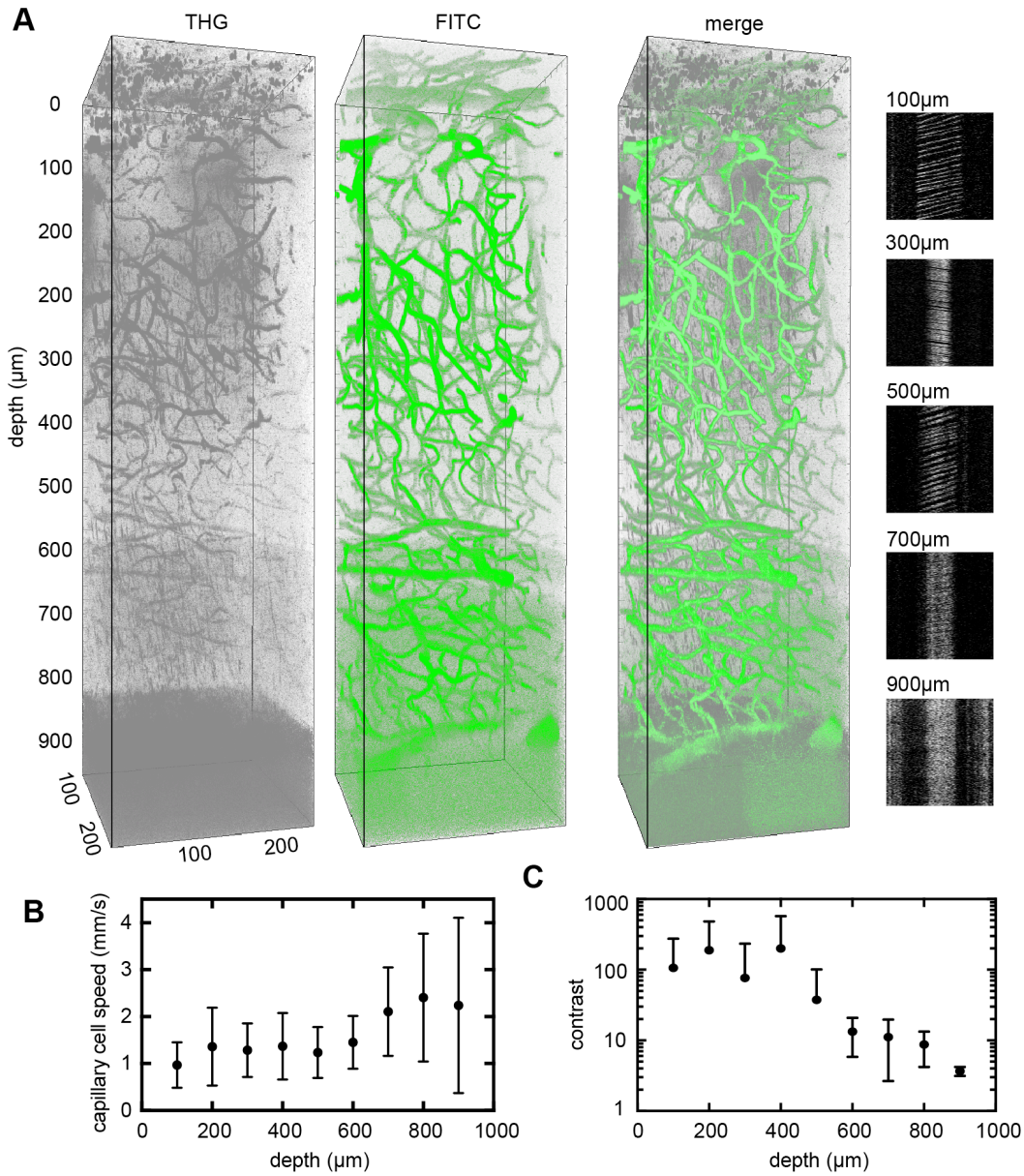

Figure 5.1 THG and FITC dextran labeled cortical vasculature up to 900μm (A) 3D rendering of THG, FITC and merged signals generated by 3PEF. Right panel shows examples of individual line scans taken at varying depths. (B) Cell speed in capillaries (diameter ~8μm) plotted as function of depth. (C) Signal to noise contrast of each set of line scan plotted as function of depth

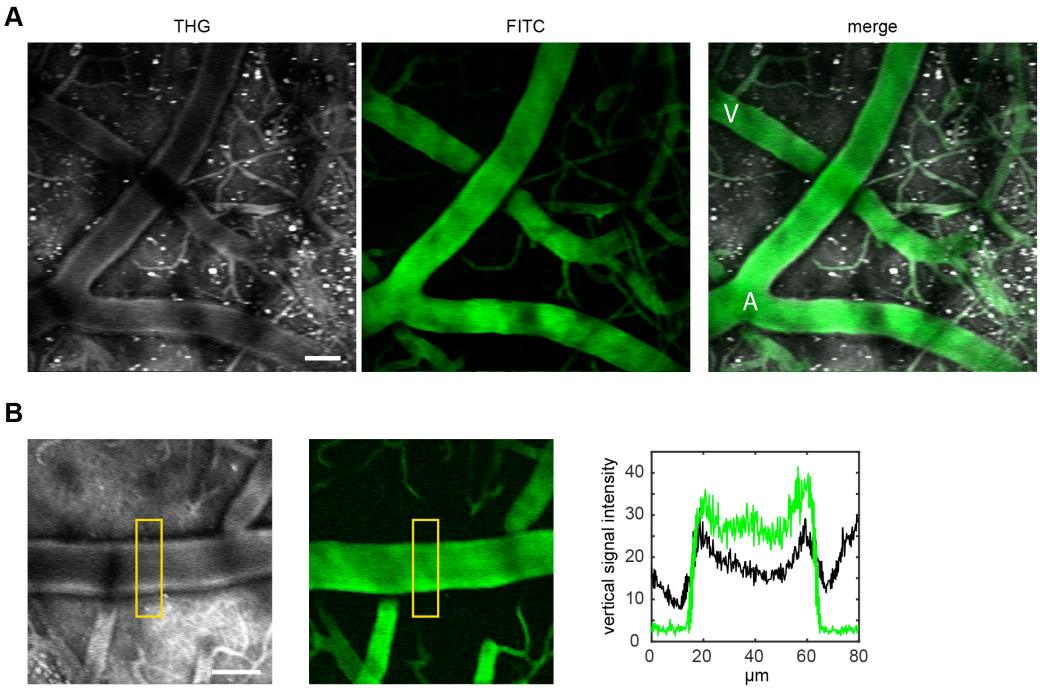

Figure 5.2 Surface cortical vessel imaging with THG and FITC dextran dye (A) Images showing thick surface vein (V) and artery (A). (**B**) Thick vessels exhibit dimmer signals in the center due to RBC absorption. All scale bars are 50μm.

identified solely by the THG produced from blood cells within the lumen. Therefore, inaccuracies may arise when measuring vessel diameter solely by THG signal. Using THG signal to measure vessel diameter produced slightly smaller results compared to 2PEF-based measurements, since THG signals cannot capture the space between the edge of the lumen and blood cells. Another disadvantage of using THG alone to identify vessels, is the possibility of missing vessels that do not have sufficient cellular flow due to temporary stalls within nearby vessels. THG imaging alone was able to identify all vessels previously identified using 3PEF of FITC dextran, except vessels within the white matter, where the THG signal from myelin dominated the entire field of view (Figure 5.4).

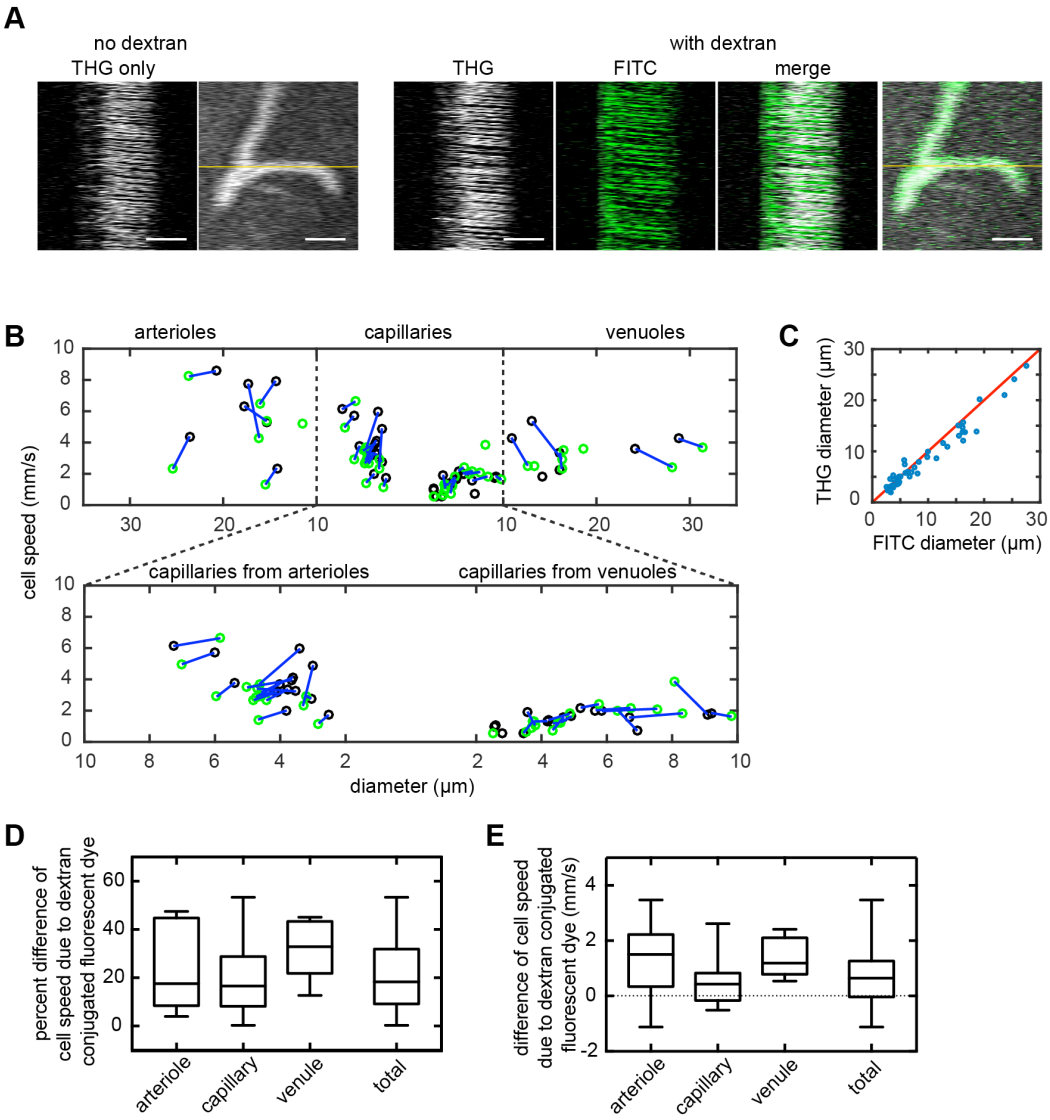

Figure 5.3 Dextran-conjugated fluorescent dyes caused cortical decreases in blood cell speed (**A**) Example showing measurement of the same vessel in different imaging sessions with (right) and without (left) dextran dye (Grey-THG, Green-FITC dextran). Scale bar is 10μm. (**B**) Cortical blood cell speed in different classes of vessels. Green dots indicate cell speed measured with FITC dextran (5% 2MDa, 100μl), black dots indicate label free cell speed measured by THG without dextran dyes. (**C**) Measured diameter of individual capillaries with FITC dextran using 2PEF and THG. (**D**) Quantitative analysis on percent decrease of blood cell speed due to FITC dextran. (**E**) Difference of cell speed with and without FITC dextran.

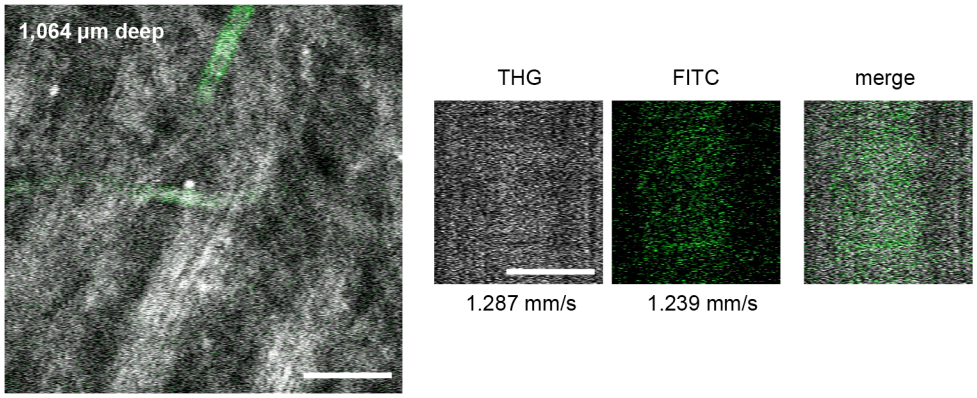

Figure 5.4 Line scan in the white matter An example of a line scan taken at the level of white matter. Scale bars are 50µm.

While measurements were similar in repeated sessions, we observed an overall systemic decrease in blood cell speed of ~20% across different classes of vessels (Figure 5.3D and E). The decrease may perhaps be due to the high molecular weight dextran.

5.4 Discussion

In this work, we demonstrated that optical phase-matching THG can provide excellent contrast for studying blood flow dynamics in the rodent brain. In the cortex, THG alone can function as an alternative to conventional labeling of blood plasma with dextran-conjugated fluorescent dyes. The sensitivity of THG in brain parenchyma was insightful since it also enabled detection of neuronal structures, although the specific neuronal subtypes could not be identified.

The use of fluorescent dextran dyes have conventionally been used to label blood plasma and to estimate blood cell speed by calculating stripes formed by time displacement of blood cells along the vessel lumen. Both the use of THG and 2PEF of FITC dextran gave clear alternating stripes in the resulting line scan images. Although THG alone can create

excellent signal contrast, accurate measurements of vessel diameter and the ability to identify vessels in the white matter may are limited, and still justify the use of dextran-conjugated dyes.

Label-free imaging holds many possibilities for various biomedical and clinical applications, since the method does not add complexity and associated risks to a system by introducing additional contrast agents. In general, most lipid structures possess third order susceptibility [15], suggesting the use of THG imaging in more applications than simply blood cell imaging, such as tumor detection, neuronal degeneration assessment, and progress of demyelination. As a result, THG microscopy may be a promising label-free tool that can be used in a wide range of applications in the biomedical field.

REFERENCE

[1] W. R. Zipfel, R. M. Williams, and W. W. Webb, "Nonlinear magic: multiphoton microscopy in the biosciences," *Nat Biotech,* vol. 21, pp. 1369-1377, 11//print 2003.

[2] V. E. Centonze and J. G. White, "Multiphoton excitation provides optical sections from deeper within scattering specimens than confocal imaging," *Biophys. J.,* vol. 75, pp. 2015-2024, // 1998.

[3] D. Kobat, M. E. Durst, N. Nishimura, A. W. Wong, C. B. Schaffer, and C. Xu, "Deep tissue multiphoton microscopy using longer wavelength excitation," *Opt Express,* vol. 17, pp. 13354-64, Aug 03 2009.

[4] E. B. Brown, "In vivo measurement of gene expression, angiogenesis and physiological function in tumors using multiphoton laser scanning microscopy," *Nat. Med.,* vol. 7, pp. 864-868, // 2001.

[5] R. H. Christie, "Growth arrest of individual senile plaques in a model of Alzheimer's disease observed by in vivo multiphoton microscopy," *J. Neurosci.,* vol. 21, pp. 858-864, // 2001.

[6] A. A. Heikal, S. T. Hess, and W. W. Webb, "Multiphoton molecular spectroscopy and excited-state dynamics of enhanced green fluorescent protein (EGFP): acid-base specificity," *Chem. Phys.,* vol. 274, pp. 37-55, // 2001.

[7] M. Stroh, W. R. Zipfel, R. M. Williams, W. W. Webb, and W. M. Saltzman, "Diffusion of nerve growth factor in rat striatum as determined by multiphoton microscopy," *Biophys. J.,* vol. 85, pp. 581-588, // 2003.

[8] N. G. Horton and C. Xu, "Dispersion compensation in three-photon fluorescence microscopy at 1,700 nm," *Biomedical Optics Express,* vol. 6, pp. 1392-1397, 2015/04/01 2015.

[9] N. G. Horton, K. Wang, D. Kobat, C. G. Clark, F. W. Wise, C. B. Schaffer*, et al.*, "In vivo three-photon microscopy of subcortical structures within an intact mouse brain," *Nat Photonics,* vol. 7, Mar 01 2013.

[10] D. A. Dombeck, L. Sacconi, M. Blanchard-Desce, and W. W. Webb, "Optical Recording of Fast Neuronal Membrane Potential Transients in Acute Mammalian Brain Slices by Second-Harmonic Generation Microscopy," *Journal of Neurophysiology,* vol. 94, pp. 3628-3636, 2005-11-01 00:00:00 2005.

[11] W. R. Zipfel, "Live tissue intrinsic emission microscopy using multiphoton-excited native fluorescence and second harmonic generation," *Proc. Natl. Acad. Sci. USA,* vol. 100, pp. 7075-7080, // 2003.

[12] Y. Barad, H. Eisenberg, M. Horowitz, and Y. Silberberg, "Nonlinear scanning laser microscopy by third harmonic generation," *Appl. Phys. Lett.,* vol. 70, pp. 922-924, // 1997.

[13] J. Squier and M. Muller, "High resolution nonlinear microscopy: A review of sources and methods for achieving optimal imaging," *Rev. Sci. Instrum.,* vol. 72, pp. 2855-2867, // 2001.

[14] D. Yelin, D. Oron, E. Korkotian, M. Segal, and Y. Silbergerg, "Third-harmonic microscopy with a titanium-sapphire laser," *Appl. Phys. B-Lasers O,* vol. 74, pp. S97-S101, // 2002.

[15] D. Débarre, W. Supatto, A.-M. Pena, A. Fabre, T. Tordjmann, L. Combettes*, et al.*, "Imaging lipid bodies in cells and tissues using third-harmonic generation microscopy," *Nature Methods,* vol. 3, p. 47, 12/20/online 2005.

[16] D. Kleinfeld, P. P. Mitra, F. Helmchen, and W. Denk, "Fluctuations and stimulus-induced changes in blood flow observed in individual capillaries in layers 2 through 4 of rat neocortex," *Proceedings of the National Academy of Sciences,* vol. 95, pp. 15741-15746, December 22, 1998 1998.

[17] C. B. Schaffer, B. Friedman, N. Nishimura, L. F. Schroeder, P. S. Tsai, F. F. Ebner*, et al.*, "Two-Photon Imaging of Cortical Surface Microvessels Reveals a Robust Redistribution in Blood Flow after Vascular Occlusion," *PLOS Biology,* vol. 4, p. e22, 2006.

[18] T. P. Santisakultarm, N. R. Cornelius, N. Nishimura, A. I. Schafer, R. T. Silver, P. C. Doerschuk*, et al.*, "In vivo two-photon excited fluorescence microscopy reveals cardiac- and respiration-dependent pulsatile blood flow in cortical blood vessels in mice," *Am J Physiol Heart Circ Physiol,* vol. 302, pp. H1367-77, Apr 01 2012.

[19] R. D. Schaller, J. C. Johnson, and R. J. Saykally, "Nonlinear chemical imaging microscopy: near-field third harmonic generation imaging of human red blood cells," *Anal Chem,* vol. 72, pp. 5361-4, Nov 01 2000.

[20] C. H. Wu, T. D. Wang, C. H. Hsieh, S. H. Huang, J. W. Lin, S. C. Hsu*, et al.*, "Imaging Cytometry of Human Leukocytes with Third Harmonic Generation Microscopy," *Sci Rep,* vol. 6, p. 37210, Nov 15 2016.

[21] A. Holtmaat, T. Bonhoeffer, D. K. Chow, J. Chuckowree, V. De Paola, S. B. Hofer*, et al.*, "Long-term, high-resolution imaging in the mouse neocortex through a chronic cranial window," *Nat Protoc,* vol. 4, pp. 1128-44, 2009.

[22] T. A. Pologruto, B. L. Sabatini, and K. Svoboda, "ScanImage: Flexible software for operating laser scanning microscopes," *BioMedical Engineering OnLine,* vol. 2, p. 13, 2003.

[23] N. Nishimura, C. B. Schaffer, B. Friedman, P. D. Lyden, and D. Kleinfeld, "Penetrating arterioles are a bottleneck in the perfusion of neocortex," *Proceedings of the National Academy of Sciences,* vol. 104, pp. 365-370, January 2, 2007 2007.

CHAPTER SIX

REDUCTION OF DEEP CORTICAL BLOOD FLOW IN APOLIPOPROTEIN 4 MOUSE

6.1 Introduction

Subcortical and periventricular white matter (WM) damage is the major pathological hallmark of vascular cognitive impairment and dementia (VCID) and AD [1-7]. However the mechanisms underlying disease progression remain unclear [8].

ApoE is a lipid transport protein that promotes lipid transport via cell surface receptors and is mainly produced by astrocytes, microglia and vascular cells in the brain [2-7]. Homozygosity for the ApoE ε4 allele (ε4/ε4) (ApoE4) is known to be correlated to WM damage, which underlies both VCID and AD [9-18]. To this date, how ApoE variants promote WM injury remains poorly understood. Much work has focused on vascular factors since ApoE ε4/ε4 individuals have reduced cerebral blood flow (CBF) and cerebrovascular reactivity [15], which could underlie the WM injury. Subcortical and periventricular WM is anatomically located at the watershed between separate arterial territories with limited collaterals, making WM particularly susceptible to ischemia. Furthermore, insufficient blood supply is known to increase susceptibility to ischemic injury [8]. Therefore, the reduction of microvascular perfusion in ApoE 4 carriers may worsen WM susceptibility to ischemic injury that may underlie cognitive impairment.

To understand the extent to which cortical and subcortical blood flow is affected with ApoE 4 allele modification, we directly measured the blood flow of ApoE 4 mice an compaed to mice carrying the human ε3 allele (ε3/ε3) (ApoE3). Furthermore, to mimic the pathological condition of reduced perfusion commonly observed in elderly populations and various disease states, we reduced brain blood flow using bilateral common carotid artery stenosis (BCAS) [19], leading to WM injury.

6.2 Methods

6.2.1 Transgenic animals We used 24 adult mice (3 - 4 month old, male) homozygous for a human ApoE3 (as control) or ApoE4 gene targeted replacement of the endogenous mouse ApoE gene (12 mice each, B6.129P2-*Apoe*$^{tm2(APOE*3)Mae}$ N8 and B6.129P2-*Apoe*$^{tm3(APOE*4)Mae}$ N8 from Taconic) [20, 21] .

6.2.2 Chronic cranial imaging window preparation A chronic cranial window was prepared using identical procedures as described in Chapter 4. Briefly, a 6-mm diameter circular bilateral craniotomy was performed over the parietal cortex on an anesthetized mouse. An 8-mm cover slip was attached and the animal was allowed to recover for a minimum of three weeks before in vivo imaging and BCAS surgery. All animal procedures were approved by the Cornell University Institutional Animal Care and Use Committee.

6.2.3 BCAS surgery Diffuse WM injury in the corpus callosum (CC) is induced by placing 0.18mm (internal diameter) microcoils on both bilateral common carotid arteries as shown in Shibata M. et al. [19]. Briefly, under 1.5~2% isofluorane anesthesia, a midline cervical incision is made and both CCAs were exposed and freed from their sheaths. Two 4–0 silk sutures were placed around the distal and proximal parts of the right CCA. Then, the artery was gently lifted by the sutures and placed between the loops of the microcoil just below the carotid bifurcation. The microcoil was twined by rotating it around the both CCA, thereby significantly reducing the diameter and compliance of the artery.

6.2.4 Multiphoton excited fluorescent microscopy Imaging was conducted using a custom multiphoton microscope. For 2PEF, a Ti:Sapphire oscillator (Chameleon, Coherent) set at 800nm was used. To generate 3PEF with 1300nm laser light, an optical parametric amplifier (OPA) (Coherent, Opera-F) was seeded by a diode-pumped femtosecond laser (60 μJ/pulse at 1 MHz; Coherent, Monaco). Dispersion for 1,300-nm excitation was compensated with an SF11 prism pair [22]. For imaging, the excitation laser was scanned with a line rate of ~1kHz with galvanometric scanners. Images were acquired with an Olympus XLPlan N 25x 1.05 NA objective. Signal was collected using custom detections optics using following emission filters (center wavelength/bandwidth): 417/60 (THG), 494/41 (FITC) separated with long-pass dichroic with cutoffs at 458nm.

6.2.5 Imaging cortical and subcortical blood flow Mice were anesthetized with isofluorane (<1.5% in oxygen) and placed in a stereotaxic apparatus equipped with a feedback-controlled heating pad. As above, mice were given atropine sulfate (0.005 mg/100 g; subcutaneously) to prevent lung secretions. The blood plasma was labeled with 2.5% w/v FITC 70 kDa conjugated dextran (Invitrogen) diluted in sterile saline and retro-orbitally injected (50 μl) before imaging. For subcortical deep imaging using 1300nm source, a more concentrated and higher volume FITC dextran (5% w/v, 100μl) was used. To quantify blood flow in subcortical vessels, we measured the vessel diameter from image stacks and the centerline RBC flow speed from line-scan measurements of THG, as described in Santisakultarm T.P. et al [23]. Respiration was monitored throughout the imaging session and the isoflurane level was adjusted to maintain a steady

breathing rate of ~1 Hz. During the imaging session, mice received an hourly dose of 5% w/v glucose in saline (1 ml/100 g) and atropine (0.001 mg/100 g) subcutaneously. All images were processed using ImageJ (National Institutes of Health), and blood cell speed was calculated by custom written MATLAB code.

6.3 Results

We used multiphoton imaging to acquire line scans of arterioles and venules on the cortical surface, capillaries branching from penetrating arterioles and ascending venules in the cortex, and other capillaries deep in the cortex and WM. Vessels were aligned to the center of the imaging field, and the speed of blood cells were captured using angled stripes as shown in Chapter 5.

We first measured baseline cortical blood flow in both ApoE 3 (as control) and ApoE 4 mice. We found no significant differences in cortical blood flow throughout classes of different cortical vessels at baseline (Figure 6.1). BCAS surgery was then performed to induce an ischemic challenge (to reduce cortical blood flow). After the BCAS procedure, there was a trend toward decreased blood flow in cortical vessels in both ApoE 3 and ApoE 4 compared to baseline (not statistically significant).

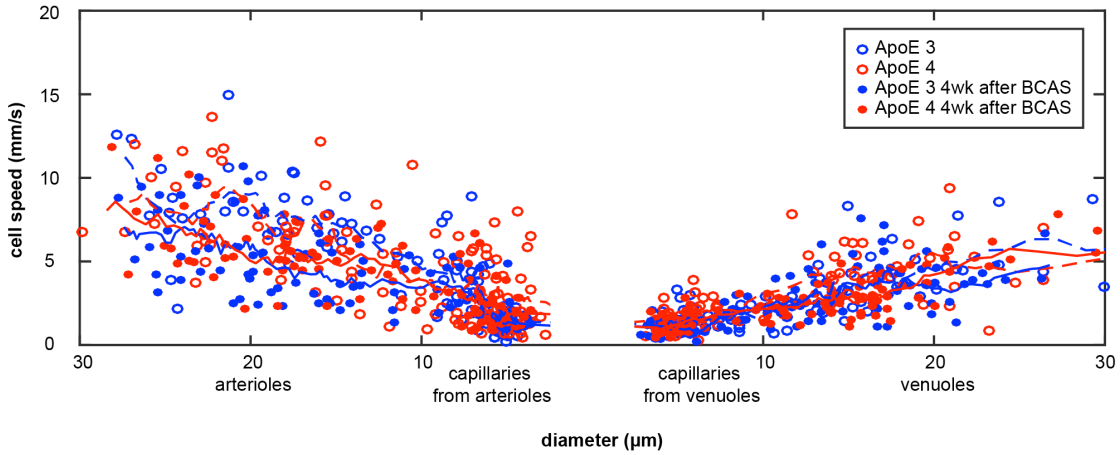

Figure 6.1 Cortical blood flow measurements in both ApoE 3 and ApoE 4 before and 4 weeks after BCAS surgery Each dot represent individual vessel line scan measurements (ApoE 3 n=167 from 4 mice, ApoE 4 n=204 from 4 mice, ApoE 3 4 weeks after BCAS n=212 from 7 mice, ApoE 4 4 weeks after BCAS n=220 from 6 mice)

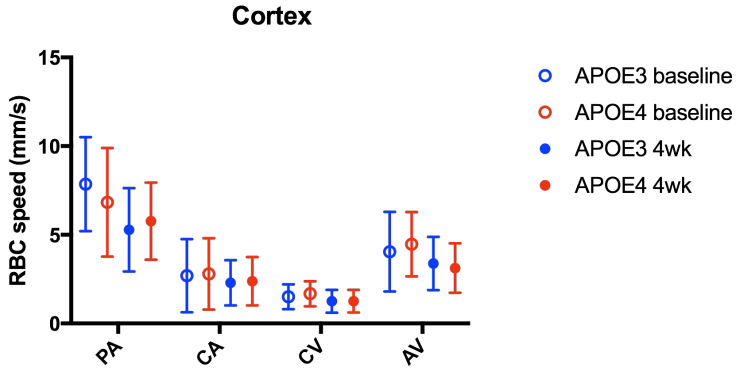

Figure 6.2 Quantification of cortical blood flow measurements before and after BCAS surgery in both ApoE 3 and ApoE 4 (same data as in Figure 6.1, categorized based on their diameter) plotted as mean and ±SD.

Using a 3PEF laser source (1300-nm excitation) allowed deeper imaging as compared to 2PEF and enabled us to visualize vessels in the WM (Figure 6.3) [24]. Higher wavelength excitation also provided additional structural information produced by THG, that is strongly produced by myelinated axons and red blood cells [25, 26]. When using 1300-

nm excitation, the THG signal was used to measure red blood cell speed instead of a fluorescent dextran, since it tends to exhibit superior contrast, as shown in Chapter five.

We next imaged flow speed of subcortical blood cells (800~1,000 μm from the surface) with 3PEF, using the same methods as above. Vessels in the WM are less curved and often align with the myelin structure, making it difficult to define vessel branch order. However most vessels are capillaries (diameter less than 10μm).

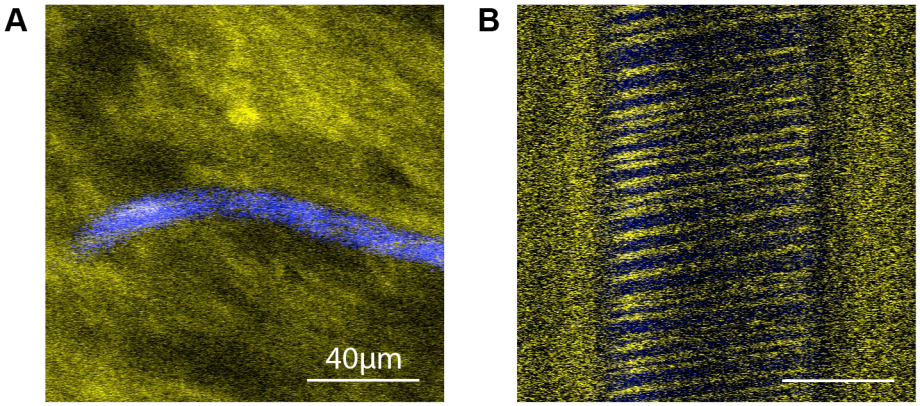

Figure 6.3 3PEF imaging of myelin structure and line scan (A) Example of capillary in the WM of the CC. Fluorescently labeled blood vessels (blue) and WM tracts (yellow, imaged via THG) (B) line scan of the capillary shown in A.

For deeper cortical measurement, almost all data were taken on capillaries since the majority of vessels in the CC WM were capillaries. Blood flow down in the WM and bottom of the cortex were also measured before and 4 wk after BCAS surgery in both ApoE 3 and ApoE 4. Blood cell speed in the WM and bottom of the cortex was reduced in ApoE 4 mice compared to ApoE 3 counterpart (Figure 6.4). After the BCAS surgery, blood flow was further reduced in both ApoE 3 and ApoE 4 expressing mice (Figure 6.4). The THG signal could also be used to visualize myelin structure and ultimately correlate myelin degeneration with blood flow changes. In the data we collected, we anecdotally

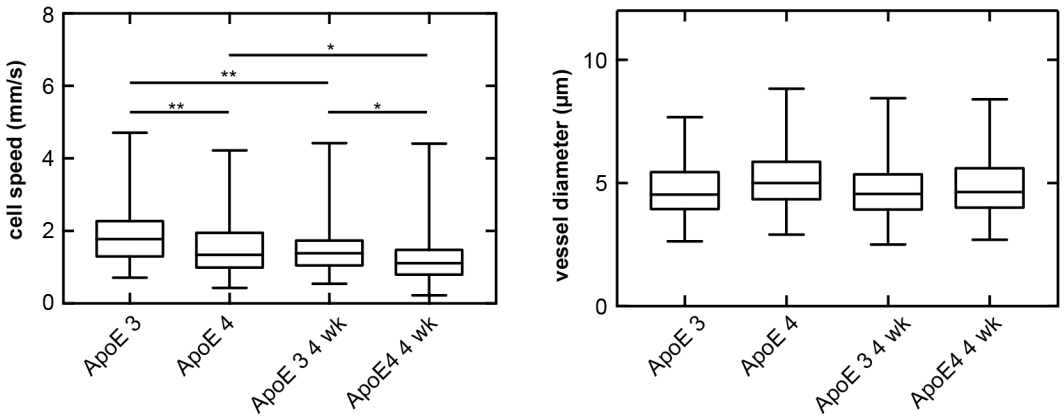

Figure 6.4 Reduced blood flow in ApoE 4 mice following BCAS surgery in deep cortex Left panel shows subcortical blood flow measurement before and 4 weeks after BCAS surgery in both ApoE 3 and ApoE 4. Right panel shows diameter of all the vessels measured in the left panel. (ApoE 3 n=81 from 4 mice, ApoE4 n=86 from 4 mice, ApoE 3 4 week after BCAS n=118 from 4 mice, ApoE 4 4 week after BCAS n=74 from 3 mice, * p value <0.005, ** p value <0.0001).

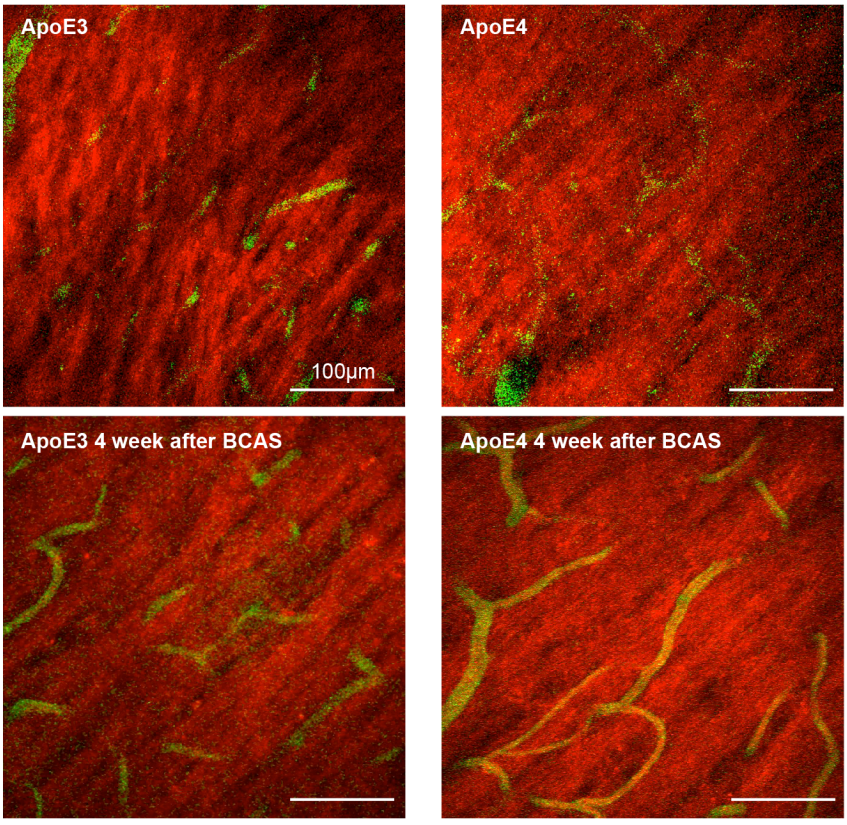

Figure 6.5 Myelin structures of ApoE3 and ApoE4 before and 4 weeks after BCAS Myelin structures are seen in red, blood vessel labeled with FITC dextran is shown in green. All scale bars are 100µm.

observed that the myelin seems in the WM seems less thick after BCAS (Figure 6.5, differences more evident in image stacks).

6.4 Discussion

ApoE 4 is known to exacerbate damage in the WM in AD, in which neurodegenerative and vascular factors coexist. However, the mechanism underlying how ApoE 4 negatively impacts the WM, in VCID that occurs in AD, remains unclear. To understand to what extent this subcortical blood flow is reduced in ApoE 4 mice without additional risk factors in relatively young mice, we directly measured the cell speed in the white matter and deep cortex. Although there was no significant change in different classes of surface cortical vessels, there was a greater reduction on the blood flow in the WM and deep cortex. This supports the possibility that neurovascular dysfunction could cause chronic ischemia in the precariously perfused deep WM via ApoE 4 directly affecting vital cerebrovascular responses that assure adequate cerebral perfusion.

REFERENCES

[1] P. B. Gorelick, A. Scuteri, S. E. Black, C. Decarli, S. M. Greenberg, C. Iadecola*, et al.*, "Vascular contributions to cognitive impairment and dementia: a statement for healthcare professionals from the american heart association/american stroke association," *Stroke,* vol. 42, pp. 2672-713, Sep 2011.

[2] C. Chai, Z. Wang, L. Fan, M. Zhang, Z. Chu, C. Zuo*, et al.*, "Increased Number and Distribution of Cerebral Microbleeds Is a Risk Factor for Cognitive Dysfunction in Hemodialysis Patients: A Longitudinal Study," *Medicine (Baltimore),* vol. 95, p. e2974, Mar 2016.

[3] T. Kanekiyo, H. Xu, and G. Bu, "ApoE and Abeta in Alzheimer's disease: accidental encounters or partners?," *Neuron,* vol. 81, pp. 740-54, Feb 19 2014.

[4] C. C. Liu, C. C. Liu, T. Kanekiyo, H. Xu, and G. Bu, "Apolipoprotein E and Alzheimer disease: risk, mechanisms and therapy," *Nat Rev Neurol,* vol. 9, pp. 106-18, Feb 2013.

[5] K. P. Koster, C. Smith, A. C. Valencia-Olvera, G. R. Thatcher, L. M. Tai, and M. J. LaDu, "Rexinoids as Therapeutics for Alzheimer's Disease: Role of APOE," *Curr Top Med Chem,* vol. 17, pp. 708-720, 2017.

[6] H. N. Yassine, M. N. Braskie, W. J. Mack, K. J. Castor, A. N. Fonteh, L. S. Schneider*, et al.*, "Association of Docosahexaenoic Acid Supplementation With Alzheimer Disease Stage in Apolipoprotein E epsilon4 Carriers: A Review," *JAMA Neurol,* vol. 74, pp. 339-347, Mar 01 2017.

[7] J. T. Yu, L. Tan, and J. Hardy, "Apolipoprotein E in Alzheimer's disease: an update," *Annu Rev Neurosci,* vol. 37, pp. 79-100, 2014.

[8] C. Iadecola, "The pathobiology of vascular dementia," *Neuron,* vol. 80, pp. 844-66, Nov 20 2013.

[9] C. Haffner, R. Malik, and M. Dichgans, "Genetic factors in cerebral small vessel disease and their impact on stroke and dementia," *J Cereb Blood Flow Metab,* vol. 36, pp. 158-71, Jan 2016.

[10] S. Schilling, A. L. DeStefano, P. S. Sachdev, S. H. Choi, K. A. Mather, C. D. DeCarli*, et al.*, "APOE genotype and MRI markers of cerebrovascular disease: systematic review and meta-analysis," *Neurology,* vol. 81, pp. 292-300, Jul 16 2013.

[11] S. Akoudad, M. de Groot, P. J. Koudstaal, A. van der Lugt, W. J. Niessen, A. Hofman*, et al.*, "Cerebral microbleeds are related to loss of white matter structural integrity," *Neurology,* vol. 81, pp. 1930-7, Nov 26 2013.

[12] L. Baum, L. C. Lam, T. Kwok, J. Lee, H. F. Chiu, V. C. Mok*, et al.*, "Apolipoprotein E epsilon4 allele is associated with vascular dementia," *Dement Geriatr Cogn Disord,* vol. 22, pp. 301-5, 2006.

[13] R. Wang, L. Fratiglioni, E. J. Laukka, M. Lovden, G. Kalpouzos, L. Keller*, et al.*, "Effects of vascular risk factors and APOE epsilon4 on white matter integrity and cognitive decline," *Neurology,* vol. 84, pp. 1128-35, Mar 17 2015.

[14] H. Schmidt, P. Freudenberger, S. Seiler, and R. Schmidt, "Genetics of subcortical vascular dementia," *Exp Gerontol,* vol. 47, pp. 873-7, Nov 2012.

[15] F. J. Wolters, R. F. de Bruijn, A. Hofman, P. J. Koudstaal, and M. A. Ikram, "Cerebral Vasoreactivity, Apolipoprotein E, and the Risk of Dementia: A Population-Based Study," *Arterioscler Thromb Vasc Biol,* vol. 36, pp. 204-10, Jan 2016.

[16] T. T. Rohn, "Is apolipoprotein E4 an important risk factor for vascular dementia?," *Int J Clin Exp Pathol,* vol. 7, pp. 3504-11, 2014.

[17] H. J. Kim, B. S. Ye, C. W. Yoon, H. Cho, Y. Noh, G. H. Kim*, et al.*, "Effects of APOE epsilon4 on brain amyloid, lacunar infarcts, and white matter lesions: a study among patients with subcortical vascular cognitive impairment," *Neurobiol Aging,* vol. 34, pp. 2482-7, Nov 2013.

[18] M. I. Kester, J. D. Goos, C. E. Teunissen, M. R. Benedictus, F. H. Bouwman, M. P. Wattjes*, et al.*, "Associations between cerebral small-vessel disease and Alzheimer disease pathology as measured by cerebrospinal fluid biomarkers," *JAMA Neurol,* vol. 71, pp. 855-62, Jul 01 2014.

[19] M. Shibata, R. Ohtani, M. Ihara, and H. Tomimoto, "White matter lesions and glial activation in a novel mouse model of chronic cerebral hypoperfusion," *Stroke,* vol. 35, pp. 2598-603, Nov 2004.

[20] P. M. Sullivan, H. Mezdour, Y. Aratani, C. Knouff, J. Najib, R. L. Reddick*, et al.*, "Targeted replacement of the mouse apolipoprotein E gene with the common human APOE3 allele enhances diet-induced hypercholesterolemia and atherosclerosis," *J Biol Chem,* vol. 272, pp. 17972-80, Jul 18 1997.

[21] C. Knouff, M. E. Hinsdale, H. Mezdour, M. K. Altenburg, M. Watanabe, S. H. Quarfordt*, et al.*, "Apo E structure determines VLDL clearance and atherosclerosis risk in mice," *J Clin Invest,* vol. 103, pp. 1579-86, Jun 1999.

[22] D. G. Ouzounov, T. Wang, M. Wang, D. D. Feng, N. G. Horton, J. C. Cruz-Hernandez*, et al.*, "In vivo three-photon imaging of activity of GCaMP6-labeled neurons deep in intact mouse brain," *Nat Methods,* vol. 14, pp. 388-390, Apr 2017.

[23] T. P. Santisakultarm, N. R. Cornelius, N. Nishimura, A. I. Schafer, R. T. Silver, P. C. Doerschuk*, et al.*, "In vivo two-photon excited fluorescence microscopy reveals cardiac- and respiration-dependent pulsatile blood flow in cortical blood vessels in mice," *Am J Physiol Heart Circ Physiol,* vol. 302, pp. H1367-77, Apr 01 2012.

[24] N. G. Horton, K. Wang, D. Kobat, C. G. Clark, F. W. Wise, C. B. Schaffer*, et al.*, "In vivo three-photon microscopy of subcortical structures within an intact mouse brain," *Nat Photonics,* vol. 7, Mar 01 2013.

[25] R. D. Schaller, J. C. Johnson, and R. J. Saykally, "Nonlinear chemical imaging microscopy: near-field third harmonic generation imaging of human red blood cells," *Anal Chem,* vol. 72, pp. 5361-4, Nov 01 2000.

[26] C. H. Wu, T. D. Wang, C. H. Hsieh, S. H. Huang, J. W. Lin, S. C. Hsu*, et al.*, "Imaging Cytometry of Human Leukocytes with Third Harmonic Generation Microscopy," *Sci Rep,* vol. 6, p. 37210, Nov 15 2016.

CHAPTER SEVEN

CONCLUTIONS AND FUTURE DIRECTIONS

In this final chapter, we will review some of the major conclusions presented in this dissertation as well as present topics where future work can be explored.

In chapter 4, we looked at the inflammatory responses after inducing a laser-induced microhemorrhage. We observed that the initial response consisted primarily of brain-resident microglia, which exhibited a coordinated pattern of migration and proliferation that led to an increased density of microglia near the lesion (primarily by migration from the surrounding tissue), while later recovering the density of microglia in the surrounding tissue (by proliferation). Reactive astrocytes were also found near the lesion with a similar spatial profile of activation as microglia, but delayed by a few days. Furthermore, a small number of invading leukocytes of different phenotypes were also observed, more inflammatory monocytes were found in earlier days and patrolling monocytes were found in later days. Although the number of invading monocytes was small, these cells were present near the lesion for days, perhaps participating in regulating the inflammatory response with brain resident glial cells.

In the resting state, microglia and astrocytes support the health and function of various neuronal populations in the brain. However, in case of small bleeds, the coordinated activation of microglia and astrocyte will occur and likely will drive potentially detremental cellular communication through inflammatory cytokines (TNF- α, IL-1β, IFN-γ) and chemicals such as ATP and nitric oxide. These signaling molecules are known to alter the strength of synaptic connectivity, affect synapse formation, and participate in maturation and elimination of neuronal spines, all of which are the

fundamental basis of neuronal plasticity. Thus, the inflammatory process we observed could, in principle, impact the function and dynamics of neural circuits by modulating plasticity. Nevertheless, our previous work with calcium imaging showed microbleeds only caused a transient loss of responsiveness to external stimuli that recovered within 4 hours after the lesion. Because neural activity in response to a peripheral stimulus may not be the most sensitive indicator of neural dysfuction, we further looked for more subtle changes in neuronal activity. Using transgenic mouse CaMKIItTA-GCamp6s that labels only excitatory neuron with a genetically-encoded calcium indicator, we sought for the changes in intrinsic firing pattern.

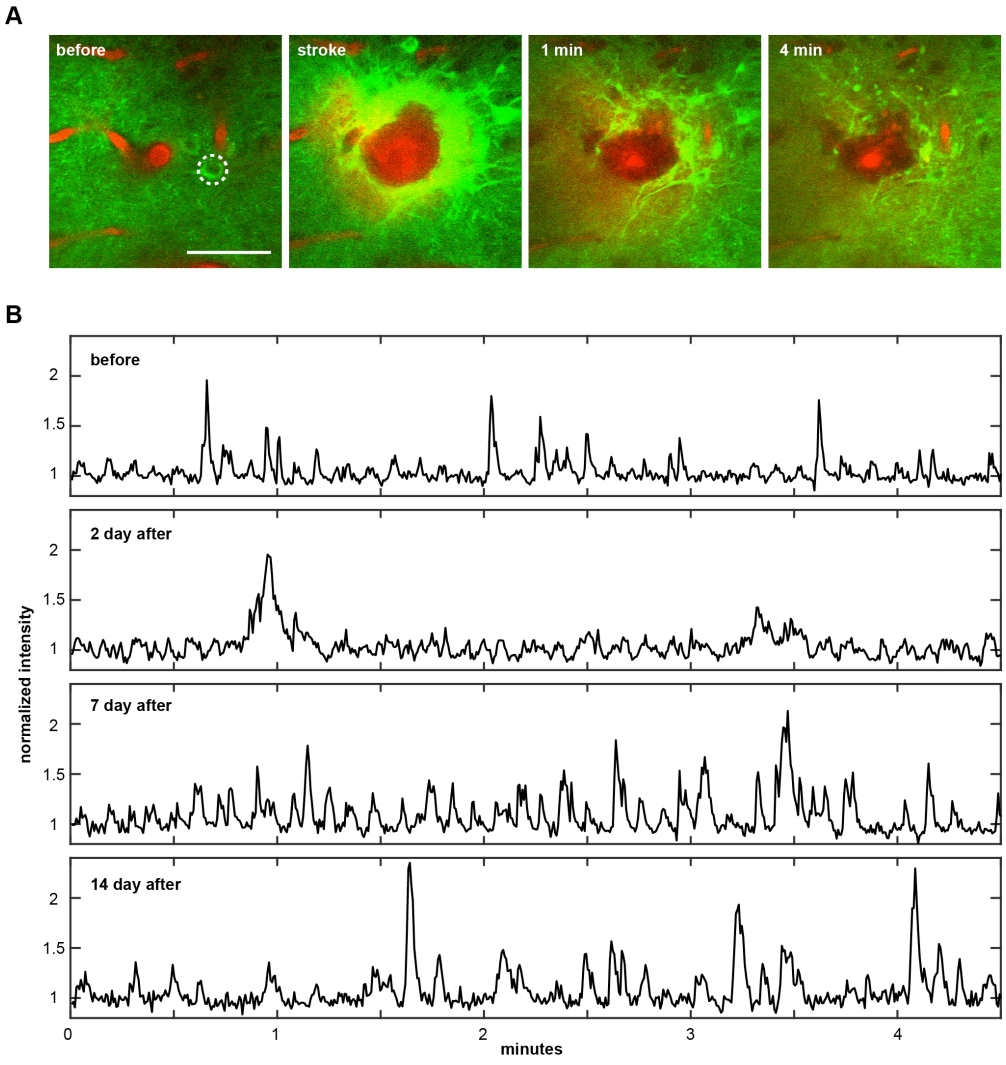

Figure 7.1 Intrinsic cellular firing pattern of nearby neurons after laser-induced microhemorrhages. (A) Images of CamKIItTA-GCamp6s mouse brain before and after the microhemorrhages (red) intravenous injected Texas red labeled blood plasma (green) calcium transients induced GFP expression. (B) Temporal profile of calcium transients from the cell circled in A.

Mice were under low level of anesthesia (<1.5% of isofluorane in medical air) and only the spontaneous calcium activity without any stimulus was recorded. Our preliminary data showed that after the onset of a microhemorrhage, excitatory neurons near the lesion (within 150 μm around the targeted vessel) had prolonged bursting activity right after the bleeding, which continued for about 2 days (Figure 7.1 B second panel). Overall firing rate was attenuated but a large population of neuron exhibited prolonged calcium transients, likely reflecting tonic bursting. In contrast, we observed increased firing rate in neurons in this same region after 7 days (Figure 7.1 B third panel).

There are many hypothesis as to why tonic bursts happen, including the view that the bursts represent a defense mechanism by neurons to overcome synaptic transmission failure as the bursts facilitate transmitter release. Inflammatory responses may or may not directly trigger these bursts by disrupting precise neurotransmitter delivery or phagocytosing synaptic spines. The next step would be looking at the relationship between these tonic bursts, or the increased firing rate we observed at later times, and the dynamic interaction of inflammatory cells activated by the microhemorrhage with neurons.

The burst firing pattern we observed itself could underlie mild cognitive decline, mood disorder, fatigue, and depression reported in patients with CMBs. Accumulation of such events and primed glial population not effectively functioning in later life, could underlie cognitive decline found in the elderly. It is still hard to find adequate methods to assess

mild cognitive decline and mental disorder in both human and animal; many topics remain to be explored.

In chapter 5, we explored the possibility of label free blood cell flow measurement. Although there were several limitation in measuring diameter with just THG, or imaging down at the WM, THG alone was sufficient to find individual vessels of interest, determine their branch orders and measure flow speed with conventional line scan techniques. We also looked for how much effect a high concentration high molecular weight dextran dye affects blood speed. We found a 20% decrease in overall cortical flow after injecting 100 μL of 5% 2 MDa FITC dextran in saline. However, the concentration typically used is smaller than what we tested, so our findings do not necessarily call into question previous work using injected dextrans, but caution is warranted. This work can therefore be a nice reference for blood flow measuring community utilizing line-scan technique, and development of label free detection tool for clinical use.

In chapter 6, we showed that ApoE 4 genotype is associated with a significant decrease in blood flow in the white matter. In surface cortical vessel we found a trend toward decreased blood flow after ischemic stress, however we didn't see significant statistical difference, possibly due to high variation between different orders of vessel branch. Furthermore, considering that there weren't any changes between groups, it does not necessarily mean that the overall blood flow is unaffected. There could still be issues with changes in vascular network due to capillaries collapsing due to ApoE4 phenotype and not be labeled or shown with the tools we used. Therefore, analysis on vascular network (number of branches and vessel density) and its structures (tortuosity) along with

further assessment on perivascular cellular components that consists different classes of vessel may deepen our understanding of changes of blood flow we observed. Moreover, myelin degeneration is often found with WM hypertention. The observation on the myelin density, functions of glial cells in the WM of ApoE 4 mice will deepen our understanding on WM lesion due to ischemic stress of ApoE 4.